Our strategy for development of platelet substitutes is straightforward; biocompatible and biodegradable carriers such as phospholipid vesicles (liposomes)[13-16] and polymerized albumin particles[17-19] are specifically accumulated at sites of vascular injury by virtue of their own mass. To construct a carrier having an accumulation ability specific to the activated GPIIb/IIIa, we conjugated an H12 sequence instead of fibrinogen to these carriers,[12,20-22] because isolated human fibrinogen is not stable.[17] We recently reported that the H12-conjugated liposomes dose-dependently reduced the bleeding time in rats with moderate thrombocytopenia in vivo.[14] However, we have not previously confirmed by in vivo studies whether the H12-liposomes are specifically accumulated at sites of vascular injury.

*N,N′*-bis[2-hydroxy-1-(hydroxylmethyl)ethyl]-5-[(2*S*)-2-hydroxypropanoylamino]-2,4,6-triiodoisophthalamide (iopamidol) is a nonionic contrast dye and is used clinically for ureterography and angiography.[23] Furthermore, it is quite easy to encapsulate iopamidol into the liposome, because iopamidol is a water-soluble contrast dye.

The purpose of this study was to visualize specific accumulation of the H12-liposomes as platelet substitutes at the sites of vascular injury. In this study we prepared H12-liposomes encapsulating iopamidol (H12-(iopamidol)liposomes), intravenously infused the H12-(iopamidol)liposomes into rats, and observed accumulation of the liposomes at jugular vein injured by ferric chloride ($FeCl_3$) and organ distribution using an eXplore Locus computed tomography (CT) system (GE Healthcare UK, Buckinghamshire, England).

## Methods

### *Materials and reagents*

1,2-dipalmitoyl-*sn*-glycero-3-phosphatidylcholine (DPPC) and cholesterol were purchased from Nippon Fine Chemical (Osaka, Japan). 1,2-distearoyl-*sn*-glycero-3-phosphatidylethanolamine-*N*-[monomethoxy poly(ethyleneglycol) (5000) (PEG-DSPE, Mn 5.1 kDa) was purchased from NOF (Tokyo, Japan). 1,5-dihexadecyl-*N*-succinyl-L-glutamate (DHSG),[24] and H12-PEG-lipid,[14] in which the fibrinogen γ-chain dodecapeptide (C-HHLGGAKQAGDV, Cys-H12) was conjugated to the maleimide group at the end of the PEG-lipids, were synthesized in our laboratory. *N,N′*-bis[2-hydroxy-1-(hydroxylmethyl)ethyl]-5-[(2*S*)-2-hydroxypropanoylamino]-2,4,6-triiodoisophthalamide (iopamidol) as a contrast dye was purchased from Fuji Pharma (Tokyo, Japan). Sephadex G25 for gel permeation chromatography was purchased from GE Healthcare UK. $FeCl_3$ was purchased from Sigma-Aldrich (St. Louis, Missouri).

### *Preparation of iopamidol-encapsulated liposomes carrying H12*

We prepared iopamidol-encapsulated liposomes carrying H12 (H12-(iopamidol)liposomes) as follows. DPPC (100 mg, 136 μmol), cholesterol (52.7 mg, 136 μmol), DHSG (18.9 mg, 27.2 μmol), PEG-DSPE (5.2 mg, 0.90 μmol), and H12-PEG-lipid (4.7 mg, 0.90 μmol) were dissolved in benzene and then freeze-dried. The resulting mixed lipids were hydrated with phosphate-buffered saline (PBS, pH 7.4) with an iopamidol adjusted to an iodine concentration of 185 mg/mL, and the resulting liposome dispersion was extruded with membrane filters (pore size: 0.80, 0.45, and then 0.22 μm, Durapore; Millipore, Tokyo, Japan). The liposomes were then washed with PBS by centrifugation (100,000*g*, 30 minutes, 4°C). The residual iopamidol was removed on Sephadex G25 (GE Healthcare UK), and the H12-(iopamidol)liposome fraction was collected. The particle diameter was analyzed by a dynamic light scattering method (N4 PLUS; Beckman-Coulter, Fullerton, Florida). Alternatively, we also prepared (iopamidol)liposomes using mixed lipids in the absence of H12-PEG-lipid.

### *Stability of the H12-(iopamidol) liposomes*

The H12-(iopamidol)liposomes at a lipid concentration of 10 mg/mL were incubated at 4°C and collected over time. After separation on Sephadex G25 (GE Healthcare UK), the H12-(iopamidol)liposome fraction was collected. The liposomes were dissolved by adding 2% (vol/vol) deca(oxyethylene) dodecyl ether (final concentration: 1% vol/vol), and the solution was heated at 42°C for 2 minutes to measure the amount of iopamidol encapsulated. Iopamidol was quantified by high-pressure liquid chromatography on a TSK-GEL ODS-100V column (TOSOH, Tokyo, Japan) with 4.6 mm outer diameter × 250 mm height using a mobile phase of 97% (vol/vol) phosphoric acid (pH 7.0) and 3% (vol/vol) methanol containing 30 mM triethylamine at 1 mL/min by the detection wavelength of 240 nm. In parallel, the lipid concentration was quantified using a commercial kit (Wako Pure Chemical Industries, Osaka, Japan).

### *CT imaging*

All animal studies were approved by the Animal Subject Committee of Keio University, School of Medicine. Male Wistar rats (250–300 g; CLEA Japan, Tokyo, Japan) were anesthetized with sodium pentobarbital at a dose of 30 mg/kg, and the H12-(iopamidol)liposomes were infused into the tail vein at a lipid dose of 130 mg/kg ([iodine] = 60 mg/kg) before induction of thrombi with $FeCl_3$. For induction of thrombus formation with $FeCl_3$, a 0.5 × 1 $cm^2$ rectangle of Whatman filter paper (GE Healthcare UK, Buckinghamshire, United Kingdom) was saturated with a 35% (wt/vol) solution of $FeCl_3$ and applied beneath the jugular vein for 30 minutes. After killing the animal the injured site was observed using an eXplore Locus computed tomography (CT) system (GE Healthcare UK). (Iopamidol) liposomes prepared without H12 ([lipid] = 130 mg/kg, [iodine] = 60 mg/kg) or iopamidol solution alone ([iodine] = 60 mg/kg) were used as control groups. We also observed the various organs 1 hour after infusion of the H12-(iopamidol)liposomes using the CT system. Each experiment was performed at least three times.

We calculated the amount of lipids accumulated at the thrombus induced with $FeCl_3$ as follows: 1 mL of the H12-(iopamidol)liposome dispersion at a range of lipid concentrations (0.25–10 mg/mL) was added to 1.5-mL tubes. After observation of the tubes by CT, the region of interest (ROI) was outlined in the tube, and the outlined volume ($mm^3$) and total

number of voxels (arbitrary unit) were calculated. From the outlined volume and a known lipid concentration in the tube, the amount of lipid in the ROI was estimated; the amount of lipid per voxel was then calculated from the amount of lipid in the ROI divided by the total number of voxels. Alternatively, the CT value per voxel was calculated from the average CT value in the ROI divided by the total number of voxels. We obtained a calibration curve of the CT value per voxel vs. the amount of lipid per voxel (ng). Finally, the amount of lipid accumulated at the injured jugular vein was calculated by extrapolation from the calibration curve of the average CT value for the total accumulation volume, from the three-dimensional (3D) image (see later discussion of Figure 3, *D*).

*Statistical analysis*

Comparisons for the H12-(iopamidol)liposome group at the injury site vs. the (iopamidol)liposome group at the injury site or the H12-(iopamidol)liposome group at the noninjury site (see later discussion of Figure 4, *B*) were carried out using Tukey-Kramer tests. A $P$ value of less than .05 was considered to be statistically significant. Statistical analyses were performed using Stat View software (Hulink, Tokyo, Japan).

## Results

Iopamidol, which is a water-soluble and nonionic contrast dye used for ureterography, was encapsulated into the inner aqueous phase of the liposome (the molar ratio of DPPC/cholesterol/DHSG = 5:5:1), and the liposome surface was modified with PEG-DSPE (0.3 mol%) and H12-PEG-lipids (0.3 mol%). Indeed, the H12-(iopamidol)liposomes were successfully prepared to homogeneity with a mean diameter of 250 ± 80 nm. The encapsulation ratios of iopamidol into the liposomes were maintained when the H12-(iopamidol)liposomes were kept at 4°C on days 0, 1, and 4. The ratios were calculated to be 100.0, 105.4, and 99.8%, respectively. Furthermore, endotoxin contamination in the liposome dispersion at a lipid concentration of 10 mg/mL was below 0.25 EU/mL, which was regarded as acceptable for an in vivo study.

First, iopamidol alone at an iodine dose of 60 mg/kg was infused into rats, and its organ distribution was observed using the eXplore Locus CT system (GE Healthcare UK). Iopamidol was rapidly excreted into the bladder via the kidney and ureter, because iopamidol is a water-soluble low-molecular-weight compound (Figure 1). It was also obvious that iopamidol did not stain blood vessels. In the case of the H12-(iopamidol)liposomes at a lipid dose of 130 mg/kg ([iodine] = 60 mg/kg) 1 hour after infusion, blood vessels and urinary organs such as kidney, ureter, and bladder showed no evidence of staining. However, liver and spleen were clearly stained (Figure 2, *A–C*), as well as (iopamidol)liposomes without H12 (data not shown). Furthermore, we confirmed that cardiac tissue was also clearly stained, suggesting that the iopamidol was stably encapsulated into the liposome, and the H12-(iopamidol)liposomes were stably circulating in blood. It was noted that encapsulation of iopamidol into the liposome changed the organ distribution from ureter and bladder to liver and spleen.

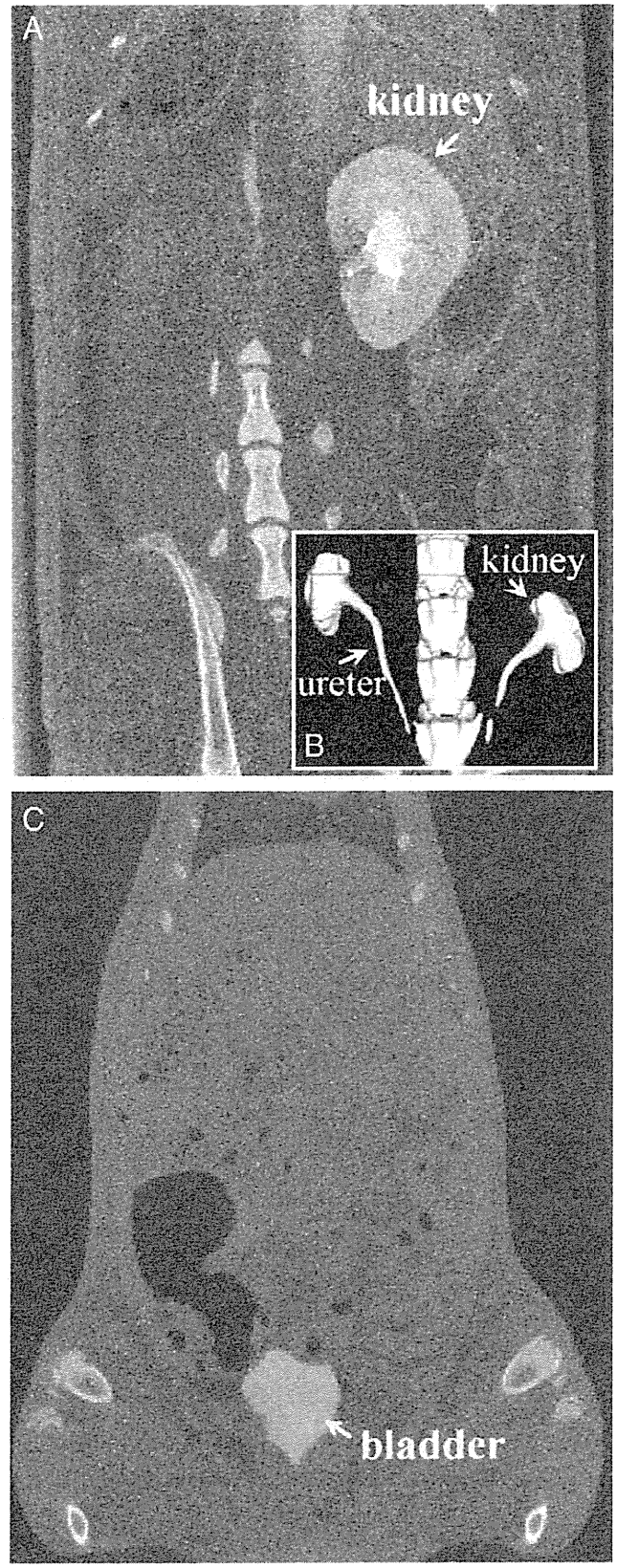


Figure 1. Abdominal CT images 5 minutes after infusion of an iopamidol solution into the rat. **(A)** Two-dimensional (2D) CT image of kidney. **(B)** 3D CT image of the kidney and ureter. **(C)** 2D CT image of the bladder. The administered amount of iopamidol was 60 mg/kg equivalent of iodine.

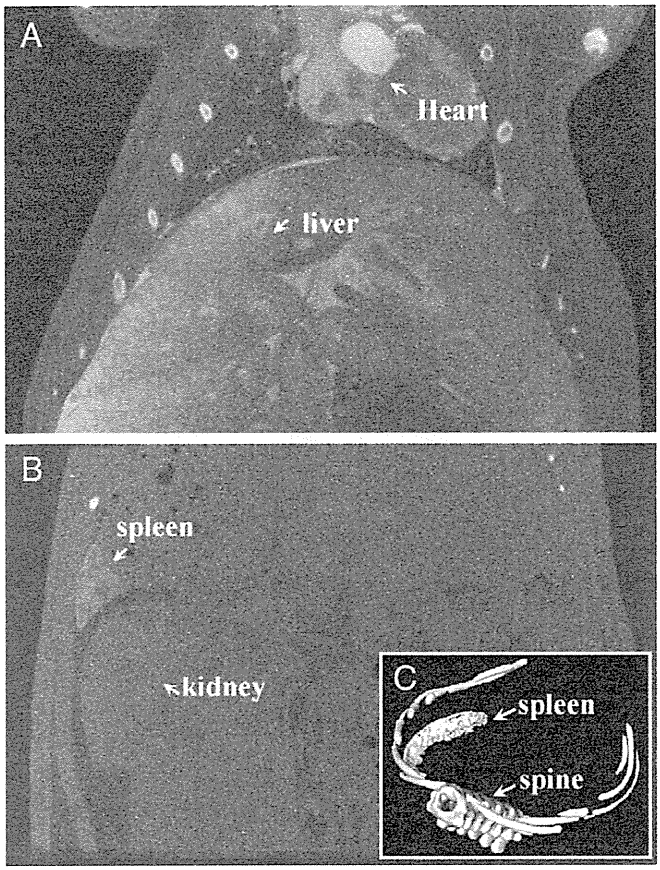


Figure 2. Abdominal CT images 60 minutes after infusion of the H12-(iopamidol)liposomes into the rat. **(A)** 2D image of the liver and heart stained with the liposomes. **(B)** 2D and **(C)** 3D CT images of the spleen stained with the liposomes. The administered amount of the H12-(iopamidol)liposomes was 130 mg/kg equivalent of lipid ([iodine] = 60 mg/kg).

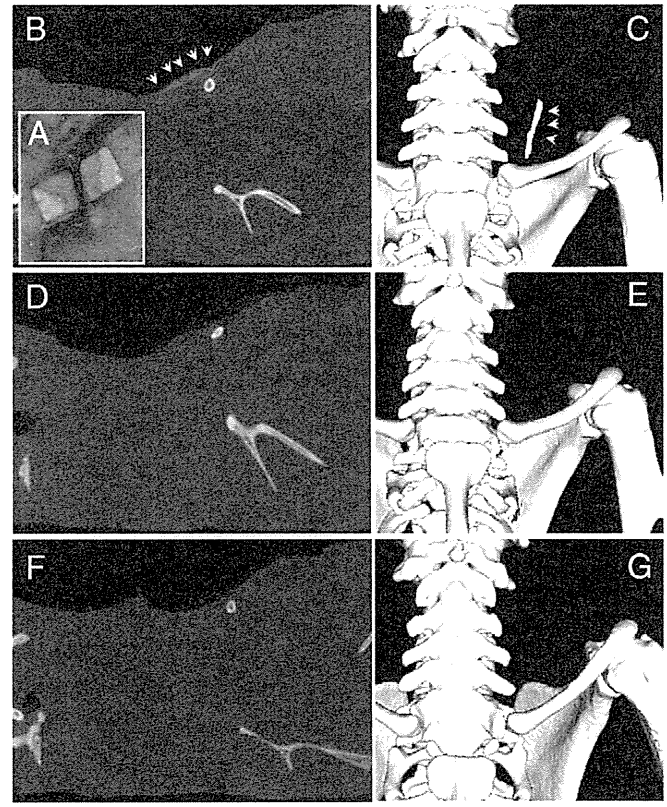


Figure 3. Specific accumulation of H12-(iopamidol)liposomes at the injury site of rat jugular vein using an eXplore Locus CT system (GE Healthcare UK). **(A)** Photograph of jugular vein on a 0.5 × 1 cm rectangle of Whatman filter paper saturated with a 35% (wt/vol) solution of $FeCl_3$ after 30 minutes. **(B)** A cross-sectional CT image of the side view of rat infused with H12-(iopamidol)liposomes. **(C)** a 3D CT image of **B**. *Arrowheads* indicate the accumulation points of the H12-(iopamidol)liposomes. **(D)** A cross-sectional CT image of the side view of rat infused with (iopamidol)liposomes. **(E)** A 3D CT image of **D**. **(F)** A cross-sectional CT image of the side view of rat infused with iopamidol solution. **(G)** A 3D CT image of **F**.

Next, we tried to visualize the accumulation of the H12-(iopamidol)liposomes at the injured sites of jugular vein. The H12-(iopamidol)liposomes at a lipid dose of 130 mg/kg ([iodine] = 60 mg/kg) were infused into the tail vein. Five minutes after infusion, a rectangle of Whatman filter paper (0.5 × 1 $cm^2$) saturated with a 35% solution of $FeCl_3$ was applied beneath the jugular vein for 30 minutes. The jugular vein turned black as shown in Figure 3, *A*, indicating that the injured jugular vein was occluded with thrombus and blood clot. It was clearly shown by the CT system that the H12-(iopamidol)liposomes accumulated at the 0.5-cm segment of jugular vein exposed to $FeCl_3$, whereas the other parts of the jugular vein were not stained (background level) as shown in Figure 3, *B*. The 3D CT image (Figure 3, *C*) also clearly shows the accumulation of the H12-(iopamidol)liposomes in the injured jugular vein. When the (iopamidol)liposomes without H12 were used there was no accumulation at the injured site (Figure 3, *D* and *E*). Furthermore, it was also clearly shown that the H12-liposomes infused intravenously were specifically accumulated to a postcaval vein exposed by $FeCl_3$ and a 1-cm length incision site of tail vein made by a no. 11 scalpel blade (data not shown). The iopamidol solution did not stain the injury site (Figure 3, *F* and *G*), because there was no mechanism for specific accumulation and iopamidol itself localized rapidly to the bladder as shown in Figure 1. Consequently, we succeeded in specific visualization of the accumulation of the H12-liposomes at the injury site using iopamidol encapsulation.

Finally, we sought to calculate the amount of lipids accumulated at the site of vascular injury. CT images of the H12-(iopamidol)liposome dispersion showed the gradation contrast images of the lipid concentration as shown in the inset of Figure 4, *A*. As indicated in the Methods section, we obtained a calibration curve with a high correlation coefficient as shown in Figure 4, *A* (the CT value per voxel vs. the amount of lipid per voxel, in nanograms). When the (iopamidol)liposomes without H12 were infused into rats the average CT value per voxel at the injury site, as shown in Figure 3, *E*, was calculated to be 163 ± 20 (Figure 4, *B*). This background level was equal to that obtained for the noninjury site (147 ± 6), suggesting that the (iopamidol)liposomes did not accumulate at the injury site. In the case of the H12-(iopamidol)liposomes as shown in Figure 3, *C*, the average CT values per voxel at the injury site were

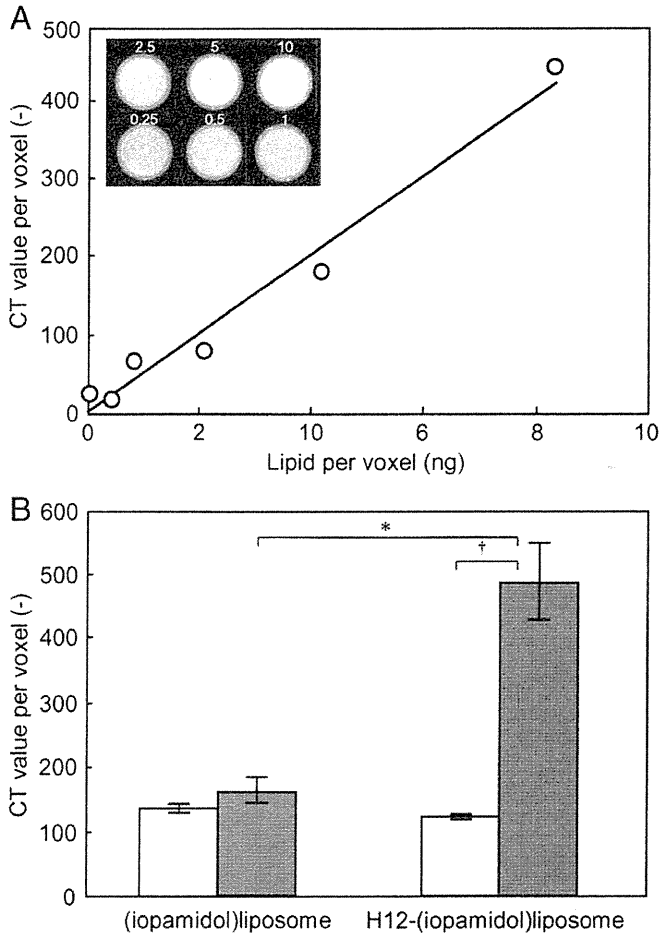


Figure 4. **(A)** Correlation of average CT values per voxel with the amount of lipid per voxel. Inset shows the CT images of the H12-(iopamidol)liposome dispersion at a lipid concentration of 0.25 to 10 mg/mL. **(B)** Average CT values per voxel at the injured jugular vein (gray columns) or noninjury site (white columns) after infusion of H12-(iopamidol)liposomes or (iopamidol) liposomes into the rats. $^{*}P < 0.05$ vs. (iopamidol)liposome group at the injury site; $^{\dagger}P < 0.05$ vs. H12-(iopamidol)liposome group at the noninjury site.

significantly increased to 489 ± 61 over that at the noninjury site (135 ± 1) (Figure 4, *B*). After extrapolation from the calibration curve of the values at the injury and noninjury sites, the amount of lipids of the H12-(iopamidol)liposomes accumulated at the injury site was estimated to be 127 ± 27 μg.

## Discussion

We confirmed elsewhere that fibrinogen γ-chain dodecapeptide (H12)-conjugated liposomes maintained the ability to specifically bind GPIIb/IIIa on the activated platelet, and that the H12-liposomes dose-dependently shortened the bleeding time of rats with moderate thrombocytopenia as a platelet substitute.[14] Our purpose in this study was to visualize the specific accumulation of the H12-liposomes at the site of vascular injury by iopamidol as a clinically used contrast dye.

We confirmed that the iopamidol was stably encapsulated into the inner aqueous phase of the H12-liposome, because of

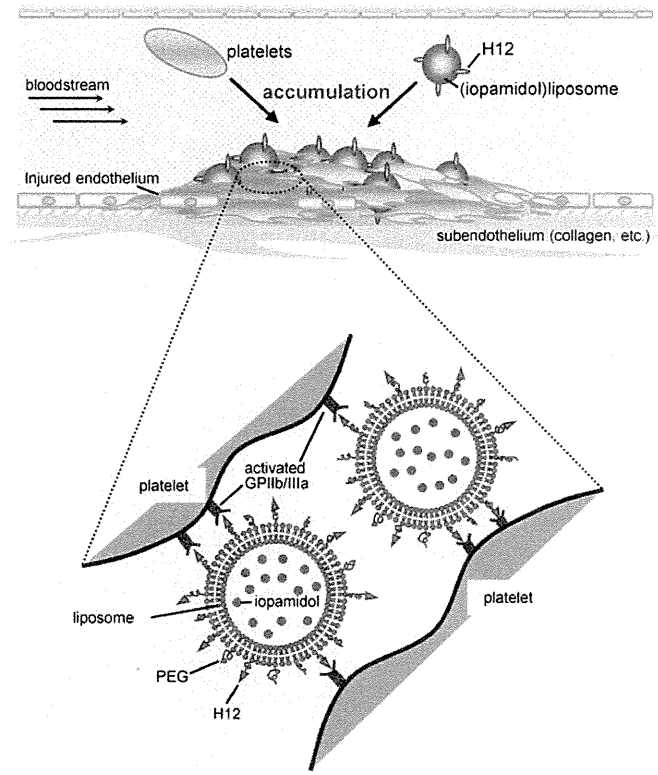


Figure 5. Schematic images of accumulation mechanism of H12-(iopamidol) liposomes at site of endothelial injury. PEG, poly(ethyleneglycol) (5000).

the stable membrane formation by DPPC and cholesterol, the electrostatic repulsion of negatively charged DHSG, and the excluding volume effect of the PEG chains on iopamidol encapsulation. By infusion of the H12-(iopamidol)liposomes into the rats, liver and spleen were shown to be clearly stained, whereas blood vessels and urinary organs such as kidney, ureter, and bladder showed no evidence of staining (Figure 2). We have already shown using a radioisotope technique that liposomes encapsulating hemoglobin as well as empty liposomes are mainly distributed in liver and spleen, and the liposomes containing hemoglobin and phospholipids readily disappeared from Kupffer cells in liver and macrophages in spleen within a week of administration to rats.[25] These are regarded as normal physiological pathways for the removal of aged erythrocytes and would also be reasonable pathways for the elimination of liposomes.[26] On the other hand, the iopamidol solution was rapidly excreted into the bladder via the kidney and ureter (Figure 1), because iopamidol is a water-soluble low-molecular-weight compound. Our experimental protocol reproduced the clinical use of iopamidol for ureterography. It was noted that encapsulation of iopamidol into the liposome changed the organ distribution from ureter and bladder to liver and spleen.

We succeeded in specific visualization of the accumulation of the H12-liposomes at the injured site using iopamidol encapsulation, based on no accumulation of the (iopamidol)liposomes without H12 and the iopamidol solution at the injured site as shown in Figure 3. This indicated that H12 on the surface of the liposome reproduced the ability to bind GPIIb/IIIa on the

activated platelet, leading to adhesion and aggregation at the site of vascular injury (Figure 5). In other words, we succeeded in detection of the platelet thrombus formation by the H12-(iopamidol)liposomes. This result provided the first direct evidence that the H12-liposomes, which dose-dependently reduced the bleeding time in thrombocytopenic rats,[14] participated in hemostasis by specific accumulation in platelet aggregates at the site of bleeding. Based on the calibration curve of the values at the injury and noninjury sites, the amount of lipids accumulated at the injury site was estimated to be 127 ± 27 μg as shown in Figure 4, corresponding to approximately 0.4% of the total amount of lipid infused into the rats (33 mg). Considering the relatively long blood circulation time (β-phase half-life of H12-liposome: 200 ± 23 minutes) and the accumulation behavior of the H12-(iopamidol)liposomes in liver and spleen as shown above, this amount of lipid accumulation at the injury site seems to be reasonable.

In conclusion, we have succeeded in visualization of the specific accumulation of H12-liposomes at a site of vascular injury using iopamidol encapsulation and CT observation, and in semiquantitative analyses of the H12-liposomes accumulated into the injured site. These results constitute direct evidence that the H12-liposomes participated in hemostasis by specific accumulation in platelet aggregates at the site of bleeding. Thus, the H12-liposomes would be promising carriers as an ideal synthetic platelet substitute that is specifically recruited to and exerts a hemostatic activity at sites of vascular injury. In another respect, it is interesting to note that the organ distribution of iopamidol itself changes from ureter and bladder to liver and spleen on encapsulation of iopamidol into the liposome. We anticipate that H12-(iopamidol)liposomes will be used clinically as diagnostic products for pathological thrombus detection and as contrast dyes for hepatosplenography, and H12-liposomes encapsulating antithrombotic drugs would be useful clinically as therapeutic agents.

## References


1. Graham SS, Gonchoroff NJ, Miller JL. Infusible platelet membranes retain partial functionality of the platelet GPIb/IX/V receptor complex. Am J Clin Pathol 2001;115:144-7.
2. Rybak M, Renzulli LA. A liposome based platelet substitute, the plateletsome, with hemostatic efficacy. Biomater Artif Cells Immobilization Biotechnol 1993;21:108-18.
3. Agam G, Livine AA. Erythrocytes with covalently bound fibrinogen as a cellular replacement for the treatment of thrombocytopenia. Eur J Clin Invest 1992;22:105-12.
4. Casals E, Verdaguer A, Tonda R, Galan A, Escolar G, Estelrich J. Atomic force microscopy of liposomes bearing fibrinogen. Bioconjug Chem 2003;14:593-600.
5. Levi M, Friedrich PW, Middleton S, De Groot PG, Wu YP, Harris R, et al. Fibrinogen-coated albumin microcapsules reduce bleeding in severely thrombocytopenic rabbits. Nat Med 1999;5:107-11.
6. Coller BS, Springer KT, Beer JH, Mohandas N, Scudder LE, Norton KJ, et al. Thromboerythrocytes: in vitro studies of a potential autologous, semi-artificial alternative to platelet transfusion. J Clin Invest 1992;89: 546-55.
7. Takagi J, Petre BM, Walz T, Springer TA. Global comformational rearrangements in integrin extracellular domains in outside-in and inside-out signaling. Cell 2002;110:599-611.
8. Xiao T, Takagi J, Coller BS, Wang JH, Springer TA. Structual basis for allostery in integrins and binding to fibrinogen-mimetic therapeutics. Nature 2004;432:59-67.
9. Mustard JF, Packham MA, Kinlough-Rathbone RL. Fibrinogen and ADP-induced platelet aggregation. Blood 1978;52:453-66.
10. Ruggeri ZM, De Marco L, Gatti L. Platelets have more than one binding site for von Willebrand factor. J Clin Invest 1983;72:1-12.
11. De Marco L, Girolami A, Zimmerman TS. Von Willebrand factor interaction with the glycoprotein IIb/IIIa complex. J Clin Invest 1986;77: 1272-7.
12. Kloczewiak M, Timmons S, Hawiger J. Localization of a site interacting with human platelet receptor on carboxy-terminal segment of human fibrinogen γ-chain. Biochem Biophys Res Commun 1982; 107:181-7.
13. Takeoka S, Teramura Y, Okamura Y, Tsuchida E, Handa M, Ikeda Y. Rolling properties of rGPIbα-conjugated phospholipid vesicles with different membrane flexibilities on vWf surface under flow conditions. Biochem Biophys Res Commun 2002;296:765-70.
14. Okamura Y, Maekawa I, Teramura Y, Maruyama H, Handa H, Ikeda Y, et al. Hemostatic effects of phospholipid vesicles carrying fibrinogen-γ chain dodecapeptide in vitro and in vivo. Bioconjug Chem 2005;16: 1589-96.
15. Kitaguchi T, Murata M, Iijima K, Kamide K, Imagawa T, Ikeda Y. Characterization of liposomes carrying von Willebrand factor-binding domain of platelet glycoprotein Ibα: A potential substitute for platelet transfusion. Biochem Biophys Res Commun 1999;261:784-9.
16. Nishiya T, Kainoh M, Murata M, Handa M, Ikeda Y. Reconstitution of adhesive properties of human platelets in liposomes carrying both recombinant glycoproteins Ia/IIa and Ibα under flow conditions: specific synergy of receptor-ligand interactions. Blood 2002;100:136-42.
17. Takeoka S, Teramura Y, Okamura Y, Handa M, Ikeda Y, Tsuchida E. Fibrinogen-conjugated albumin polymers and their interaction with platelets under flow conditions. Biomacromolecules 2001;2:1192-7.
18. Okamura Y, Takeoka S, Teramura Y, Maruyama H, Tsuchida E, Handa M, et al. Hemostatic effects of fibrinogen γ-chain dodecapeptide-conjugated polymerized albumin particles in vitro and in vivo. Transfusion 2005;45:1221-8.
19. Okamura Y, Fujie T, Maruyama H, Handa M, Ikeda Y, Takeoka S. Prolonged hemostatic ability of poly(ethylene glycol)-modified polymerized albumin particles carrying fibrinogen γ-chain dodecapeptide. Transfusion 2007;47:1254-62.
20. Kloczewiak M, Timmons S, Lukas TJ, Hawiger J. Platelet receptor recognition site on human fibrinogen: synthesis and structure-function relationship of peptides corresponding to the carboxy-terminal segment of the γ chain. Biochemistry 1984;23:1767-74.
21. Kloczewiak M, Timmons S, Bednarek MA, Sakon M, Hawiger J. Platelet receptor recognition domain on the γ chain of human fibrinogen and its synthetic peptide analogues. Biochemistry 1989;28:2915-9.
22. Lam SC, Plow EF, Smith MA, Andrieux A, Ryckwaert JJ, Marguerie G, et al. Evidence that arginyl-glycyl-aspartate peptides and γ chain peptides share a common binding site on platelets. J Biol Chem 1987; 262:110-5.
23. Langheinrich AC, Ritman EL. Quantitative imaging of microvascular permeability in a rat model of lipopolysaccharide-induced sepsis. Invest Radiol 2006;41:645-50.
24. Takeoka S, Mori K, Ohkawa H, Sou K, Tsuchida E. Synthesis and assembly of poly(ethylene glycol)-lipids with mono-, di-, tetraacyl chains and a poly(ethylene glycol) chain of various molecular weights. J Am Chem Soc 2000;122:7927-35.
25. Sou K, Klipper R, Goins B, Tsuchida E, Phillips WT. Circulation kinetics and organ distribution of Hb-vesicles developed as a red blood cell substitute. J Pharmacol Exp Ther 2005;312:702-9.
26. Sakai H, Horinouchi H, Tomiyama K, Ikeda E, Takeoka S, Kobayashi K, et al. Hemoglobin-vesicles as oxygen carriers: influence on phagocytic activity and histopathological changes in reticuloendothelial system. Am J Pathol 2001;159:1079-88.

Original Article

# Characteristic Changes in Heart Rate Variability Indices during Hemorrhagic Shock, and Effect of Liposome-Encapsulated Hemoglobin in Rats

Yashiro Nogami MD*4, Bonpei Takase MD*1, Manabu Kinoshita MD*3, Satoshi Shono MD*4, Shinichi Kaneda PhD*6, Masayuki Ishihara PhD*2, Makoto Kikuchi PhD*5, Tadaaki Maehara MD*4

*1Department of Intensive Care Medicine, National Defense Medical College
*2Divisions of Biomedical Engineering, National Defense Medical College Research Institute
*3Departments of Immunology and Microbiology, National Defense Medical College
*4Department of Surgery, National Defense Medical College
*5Department of Medical Engineering, National Defense Medical College
*6Terumo Corporation R&D Center

Many compensatory mechanisms exit in hemorrhagic shock (HS). To characterize the efficacy of the new artificial oxygen carrier, liposome-encapsulated hemoglobin (LHb), HS was induced by withdrawing 20% of the total blood volume from rats. Rats received one of five interventions: LHb resuscitation (LHb-G, n = 7), normal saline (Saline-G, n = 7), shed autologous blood (SAB-G, n = 7), volume expander of 5% albumin (Albumin-G, n = 7), or no treatment (Sham-G, n = 7). Heart rate variability (HRV) indices were measured, including low frequency (LF, 0.10–0.60 Hz), high frequency (HF, 0.60–2.00 Hz), and the ratio of LF to HF (LF/HF). LF and LF/HF following HS were lower in the LHb-G and SAB-G groups when compared with the Saline-G, Albumin-G and Sham-G groups. LF and LF/HF following HS in the LHb-G group were comparable with that of the SAB-G group. These data demonstrate that HS-induced changes can be attenuated by resuscitation with LHb as well as SAB. LHb could be used as a substitute for blood transfusion for HS.
(J Arrhythmia 2010; 26: 189–198)

**Key words:** Bleeding, Red blood cell, Resuscitation, Autonomic nervous system

## Introduction

Many compensatory mechanisms participate in the response to hemorrhagic shock, including neurohormonal factors[1–3] mediated by pressure receptors and chemoreceptors,[4–6] and increases in sympathetic nervous system activity. Heart rate variability (HRV) is a well known index that reflects the autonomic control of the heart,[7,8] but changes in HRV in response to hemorrhagic shock remain unclear.

Hemoglobin (Hb)-based $O_2$ carriers (HBOCs) have been developed as a substitute for red blood

*Received 10, November, 2009: accepted 1, July, 2010.*
Address for correspondence: Bonpei Takase MD, National Defense Medical College, Department of Intensive Care Medicine, 3-2 Namiki, Tokorozawa, Saitama 359-8513, Japan. Phone: 011-81-42-995-1618 Fax: 011-81-42-925-0967 E-mail: bonpeit@ndmc.ac.jp dui1577@db3.so-net.ne.jp

cells and some of them are currently in clinical trials as oxygen therapeutics.[9–11] HBOCs are classified into two categories; one is acellular Hb (polymerized Hb, cross-linked Hb, PEG-modified Hb) and the other is cellular Hb (liposome-encapsulated Hb hemoglobin vesicles). It has been reported that the acellular Hbs have a pressor effect on peripheral vessels as nitric oxide (NO) scavengers, and subsequent harmful effects on the microcirculationm, because the acellular Hbs have a high affinity to NO and thereby they combine with NO in the vessel lumen and/or in the interstitial space after extravasation of the acellular Hb.[12,13] In contrast, the cellular Hbs have lipid bilayer membranes (liposome) that prevent direct contact with blood components and endothelium so that cellular Hbs can attenuate this pressor effect of acellular Hbs.[14]

Recently, the use of an artificial oxygen carrier composed of polyethylenglycol-modified liposome-encapsulated hemoglobin (LHb), which is classified as the cellular Hbs, has been demonstrated to be beneficial in the treatment of hemorrhagic shock in animal models.[15–17] Further, this artificial oxygen carrier may significantly affect changes in HRV during hemorrhagic shock through its salutary effect on the autonomic nervous system.

Therefore, the goal of the present study was to investigate the influence of hemorrhagic shock on autonomic nervous system activity assessed by HRV and to characterize the therapeutic efficacy of the newly developed artificial oxygen carrier, LHb, in an animal model of hemorrhagic shock.

## Methods

All animal procedures were conducted in accordance with guidelines published in the Guide for the Care and Use of Laboratory Animals (DHEW publication NIH 85-23, revised 1996, Office of Science and Health Reports, DRR/NIH, Bethesda, MD, USA). The study protocol was approved by the Committee on Animal Research of the National Defense Medical College.

### 1. Materials and experimental preparation

Experiments were performed using 35 male Sprague Dawley rats (weight range, 270–350 g; mean weight, 310 g; Tokyo Laboratory Animal Science, Tokyo, Japan). All rats were housed in cages and provided with food and water *ad libitum* in a temperature-controlled room on a 12-hr dark/light cycle. Rats were anesthetized by intraperitoneal administration of sodium pentobarbital (50 mg/kg body weight) and then allowed to stabilize under spontaneous respiration on a heating blanket to maintain a body temperature 37–38 °C. Needle-type electrodes were inserted into the subcutaneous area in both the front and hind limbs in order to continuously record the electrocardiogram (ECG). The left femoral artery and vein were cannulated with polyethylene indwelling needles (27G, Terumo, Co., Tokyo, Japan). Needles were placed into the femoral artery and connected to a fluid-filled manometer (ADInstrument BPump Utah Medical Products Inc., Utah, USA) to monitor blood pressure. ECG and blood pressure were continuously monitored and recorded using a commercial laboratory catheter system (RMC-3100, CardioMaster, Nihon-Koden Inc., Tokyo, Japan).

LHb[1] was provided by Terumo Corp. (Tokyo, Japan). Features of LHb are briefly summarized as follows: LHb was made of stroma-free hemoglobin solution, which was obtained from outdated human red blood cells and encapsulated by liposomes (diameter, 220 nm). The surfaces of encapsulated liposomes were modified with 5-kDa polyethylenglycol in order to attenuate aggregation. LHb was diluted with saline to 6 g/dl Hb in concentration. The $P_{50}$ (a measure of $O_2$ tension when the Hb binding sites are 50% saturated) was adjusted to 40–50 mmHg by adding inositol hexaphosphate.[18]

#### 1) Hemorrhagic shock resuscitated with LHb, normal saline and shed autologous blood (SAB)

The arterial line was used to induce hemorrhagic shock by withdrawing 20% of systemic blood volume over a period of 2 min from the femoral artery. Systemic blood volume was estimated at 5.6% of total body weight (56 ml/kg). Five minute later, the same volume of LHb (LHb group, n = 7), normal saline (0.9% NaCl; Saline group; n = 7) and SAB (SAB group, n = 7) was infused through the femoral vein for resuscitation. Seven rats did not receive resuscitative treatment (Sham group).

#### 2) Hemorrhagic shock resuscitated with either LHb or volume expander

In order to separately evaluate the effect of LHb's oxygen carrying and volume expanding properties during hemorrhagic shock, the following experiment was additionally conducted. The arterial line was also used to induce hemorrhagic shock by withdrawing 20% of systemic blood volume over a 2 min period from the femoral artery. Five minutes later, the same volume of a 5% albumin volume expander (Albumin group, n = 7) was infused through the femoral vein for resuscitation. The Albumin group was compared with the LHb-resuscitated group

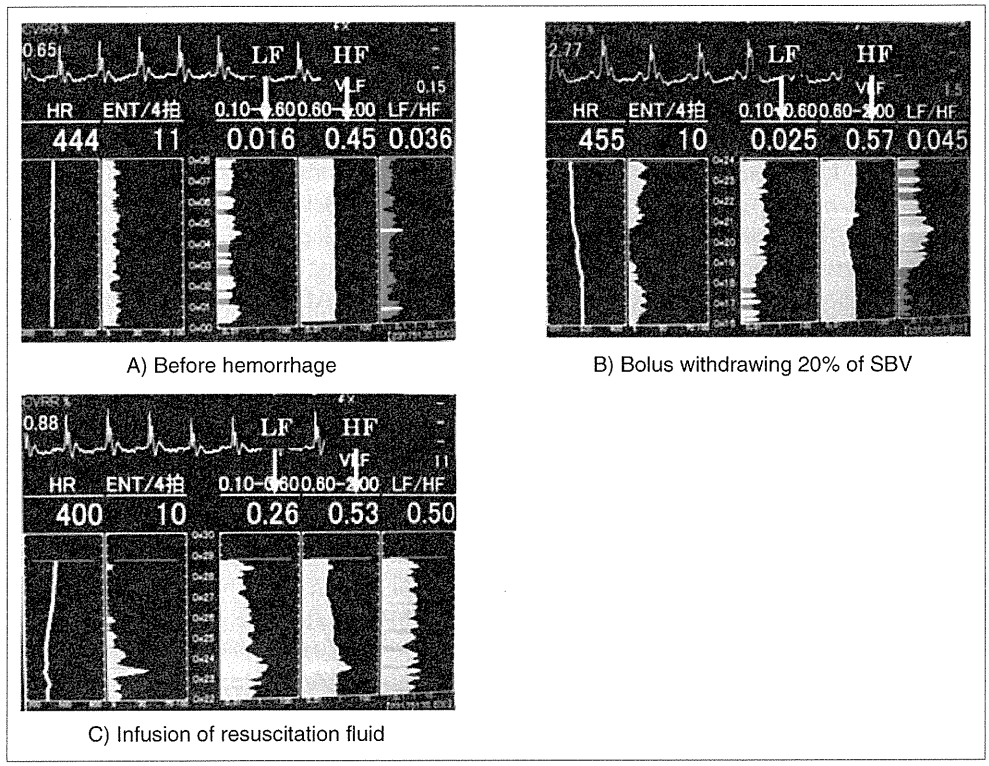


**Figure 1**
Typical real tracings of heart rate variability indices before hemorrhage (**A**), bolus withdrawing 20% of systemic blood volume (SBV, **B**) and infusion of resuscitation fluid (**C**).
LF: low frequency spectra, HF: high frequency spectra, LF/HF: LF/HF ratio

prepared using the same method as previously described (n = 7).

2. Measurement of the HRV indices and experimental protocol

RR intervals were transferred to a personal computer, and HRV indices were measured with commercialized software (MemCalc/Tarawa, Suwa Trust Inc., Tokyo, Japan) based on the RR intervals of normal sinus beats obtained from the ECG throughout the entire study period as previously reported[19] and sampling frequency of ECG for measuring HRV indices was 1000 Hz. For the frequency domain analysis, online analysis was performed for five consecutive RR intervals using the modified Maximum Entropy Method. Low frequency spectra (LF, 0.10–0.60 Hz), and high frequency spectra (HF, 0.60–2.00 Hz) were continuously calculated. Thereafter, these values were averaged over the subsequent 5 min from time points that are described later. The ratio of low frequency spectra and high frequency spectra was also measured as the LF/HF ratio. Heart rate, blood pressure, and HRV indices were measured immediately before hemorrhage (Pre), immediately after hemorrhage (After bleeding), immediately after resuscitation with LHb, normal saline, SAB or 5% albumin infusion (Just after infusion), and 15 min, 30 min, 45 min and 60 min after resuscitation as shown in **Figure 1**.

All these experimental procedures were performed during day time between 09:00 and 17:00 (light cycle).

3. Statistics

Data are expressed as mean ± SEM if not otherwise indicated. Student's t-test was used to compare heart rate, blood pressure, and HRV indices between two groups. Data among three groups were compared by ANOVA with Scheffe's correction. Temporal changes in each parameter were compared by repeated calculation of ANOVA if not otherwise indicated. $P < 0.05$ was considered to represent statistical significance.

## Results

1. Hemorrhagic shock resuscitated with LHb, normal saline and SAB compared with Sham group

Induction of hemorrhagic shock resulted in a decrease in mean blood pressure to almost same

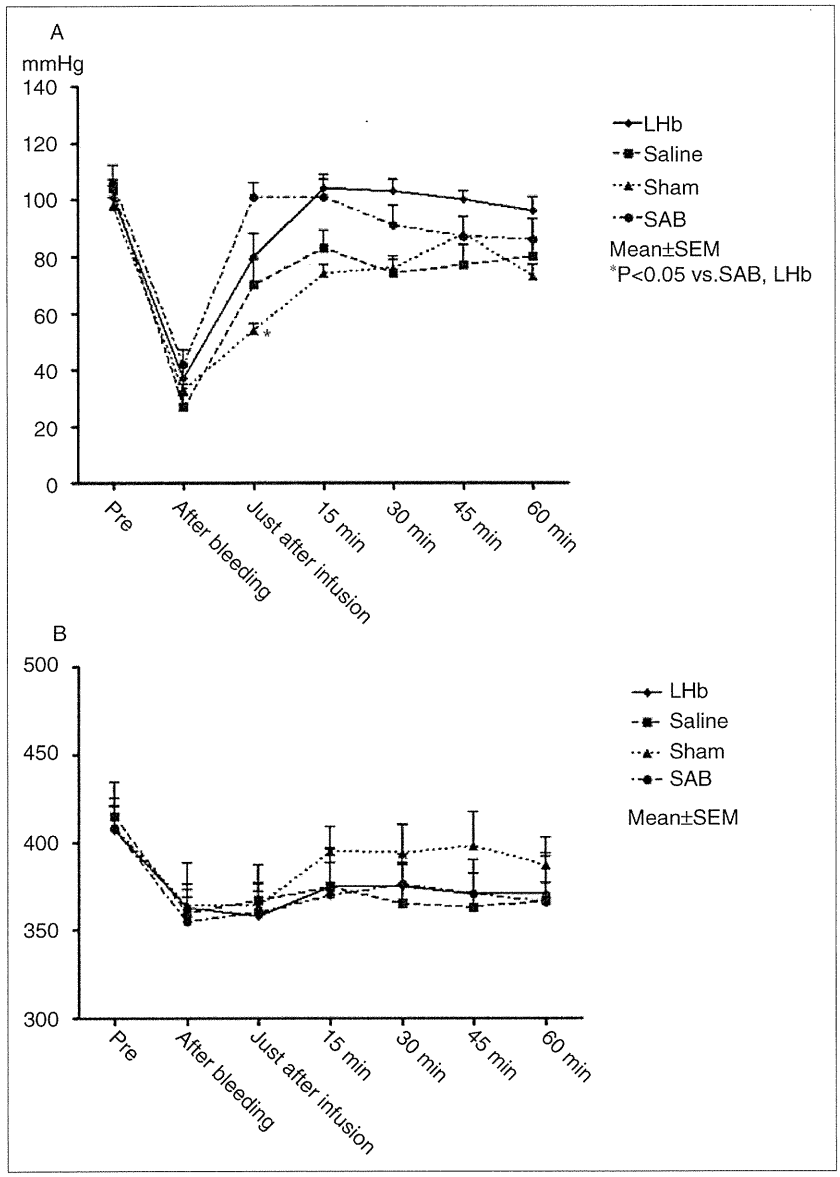


**Figure 2**
Temporal changes in mean blood pressure (mmHg; panel **A**) and heart rate (beats/min; panel **B**) are illustrated in hemorrhagic shock resuscitated with polyethylenglycol-modified liposome-encapsulated hemoglobin (LHb), normal saline (Saline) and shed autologous blood (SAB), and also in hemorrhagic shock without resuscitation (Sham group).
LHb: LHb group, Saline: Saline group, Sham: Sham group, SAB: SAB group, Data are expressed as mean ± SEM, Pre: values measured immediately before hemorrhage, After bleeding: values measured immediately after hemorrhage, Just after infusion: values measured immediately after resuscitation with each infusion, 15 min, 30 min, 45 min and 60 min are indicated as time elapsed after resuscitation.

degree around from 101 ± 2 mmHg to 35 ± 2 mmHg in all four groups (**Figure 2-A**). Resuscitation resulted in an abrupt increase in mean blood pressure to 80 ± 8 mmHg, 70 ± 8 mmHg and 101 ± 5 mmHg in the LHb, Saline and SAB groups, respectively (**Figure 1-A**). Animals in the Sham group showed spontaneously gradual recovery in blood pressure despite the absence of resuscitative interventions. When the temporal change in mean blood pressure was compared, mean blood pressure in LHb and SAB groups tended to be higher than those of the other two groups. There was no significant difference in shock-induced changes in heart rate when comparing the three intervention groups (**Figure 2-B**).

Temporal changes in HRV indices are shown in **Figures 3-A, B, C**. Induction of hemorrhagic shock resulted in significant and similar increases in LF spectra in all four groups (**Figure 2-A**). After resuscitation or spontaneous recovery, the value of the LF spectra in both Saline and Sham groups gradually and significantly increased, whereas the value of the LF spectra in the LHb and SAB group remained low. As a result, the values of LF spectra at 60 min after resuscitation was significantly lower in the LHb and SAB groups than in the Sham and Saline groups ($0.04 \pm 0.01\ ms^2/Hz$, $0.02 \pm 0.01\ ms^2/Hz$ vs. $0.22 \pm 0.08\ ms^2/Hz$ and $0.12 \pm 0.03\ ms^2/Hz$, $P < 0.05$). Further, values of the HF spectra tended to be higher in the LHb and SAB groups when

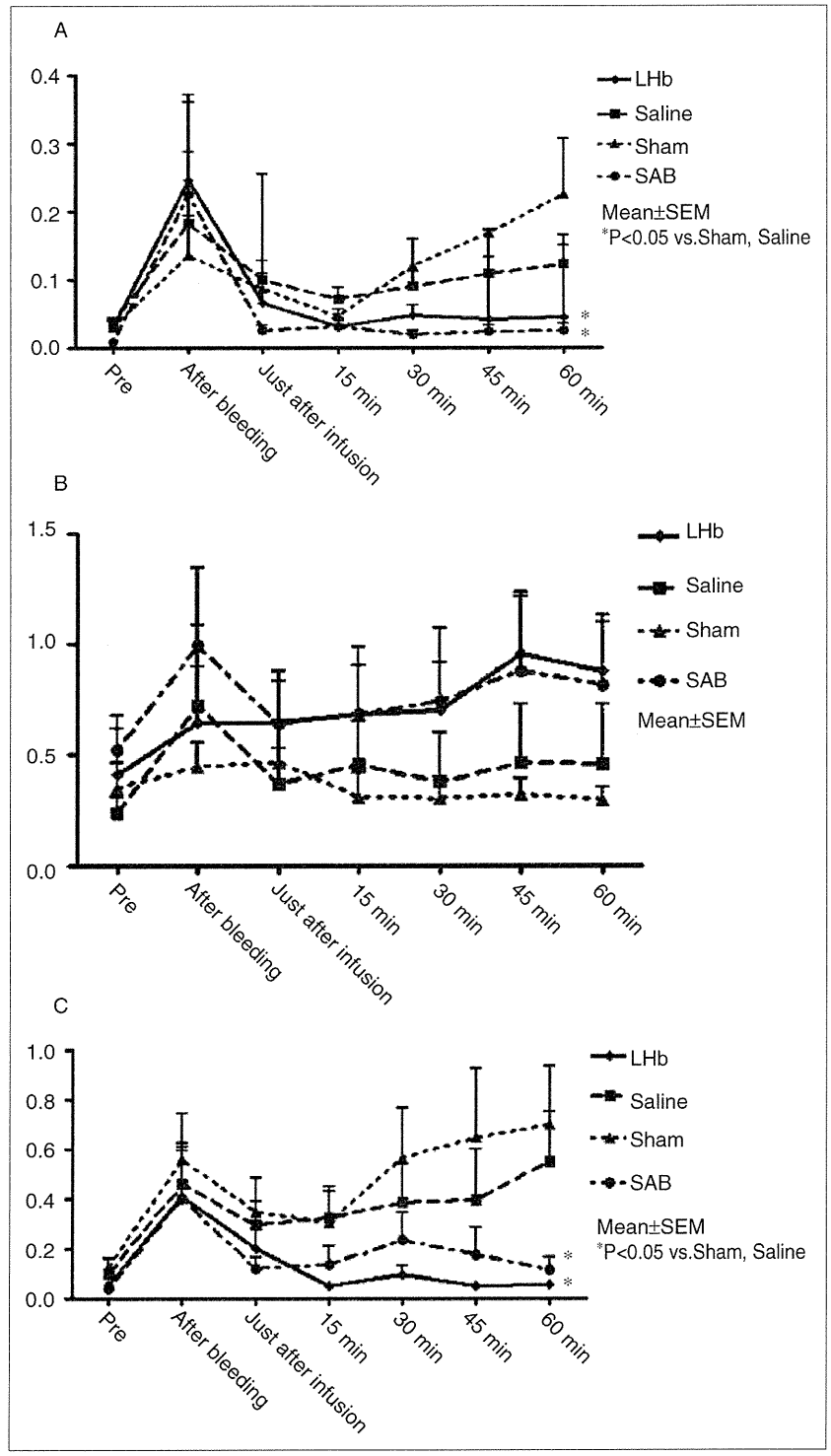


**Figure 3**
Temporal changes in low frequency spectra (LF, $ms^2/Hz$; panel **A**), high frequency spectra (HF $ms^2/Hz$; panel **B**), and LF/HF ratio (panel **C**) in hemorrhagic shock resuscitated with polyethylenglycol-modified liposome-encapsulated hemoglobin (LHb), normal saline (Saline) and shed autologous blood (SAB), and also in hemorrhagic shock without resuscitation (Sham group).
Format and abbreviations are identical to those in Figure 2.

compared with the Sham and Saline groups at most time points, but this difference did not reach the level of statistical significance (**Figure 3-B**). The LF/HF ratio after resuscitation tended to be lower in the LHb and SAB groups when compared with the Sham and Saline groups (**Figure 3-C**). Further, the LF/HF ratio at 60 min after resuscitation was significantly lower in the LHb and SAB groups than in the Sham and Saline groups ($0.05 \pm 0.01$, $0.11 \pm 0.05$ vs $0.60 \pm 0.27$, $0.48 \pm 0.18$, $P < 0.05$).

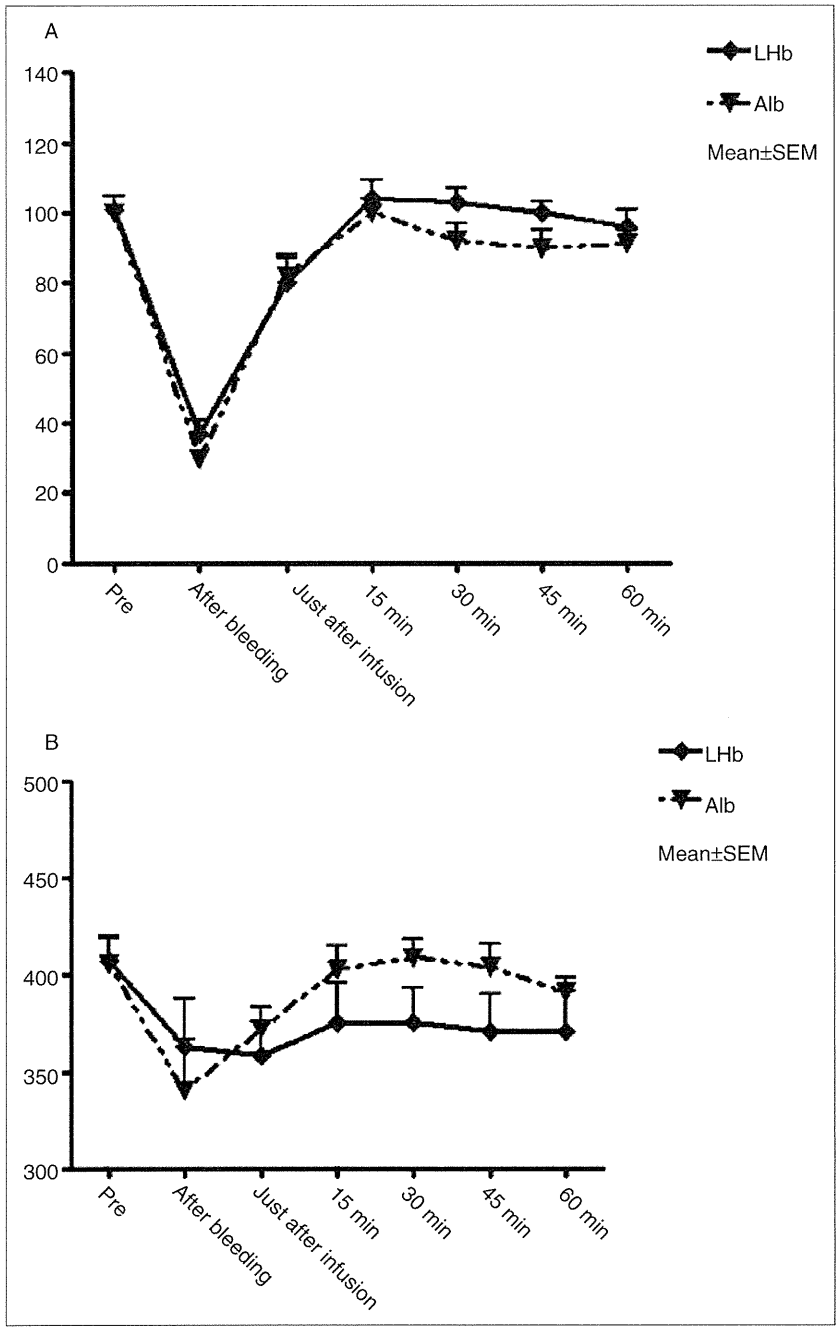


**Figure 4**
Temporal changes in mean blood pressure (mmHg; panel **A**) and heart rate (beats/min; panel **B**) are illustrated in hemorrhagic shock resuscitated with either polyethylenglycol-modified liposome-encapsulated hemoglobin (LHb) or volume expander of 5% albumin.
LHb: LHb group, Alb: Albumin group, Data are expressed as mean ± SEM, Pre: values measured immediately before hemorrhage, After bleeding: values measured immediately after hemorrhage, Just after infusion: values measured immediately after resuscitation with each infusion, 15 min, 30 min, 45 min and 60 min are indicated as time elapsed after resuscitation.

2. Hemorrhagic shock resuscitated with volume expander

To compare the effect of volume expander with that of LHb, the same data described above were used for LHb group. Induction of hemorrhagic shock resulted in a decrease in mean blood pressure to almost same degree (from 100 ± 3 mmHg to 35 ± 3 mmHg) in the two groups (LHb and Albumin groups). In the LHb and albumin groups, resuscitation resulted in an abrupt increase in mean blood pressure to 80 ± 8 mmHg and 82 ± 5 mmHg, respectively (**Figure 4-A**). There was no significant difference in shock-induced changes in heart rate when comparing the two groups (**Figure 4-B**). Temporal changes in HRV indices are shown in **Figures 5-A, B, C**. The LF after resuscitation tended to be lower in the LHb group than the Albumin group. Further, the LF at 60 min after resuscitation was significantly lower in the LHb group than in the Albumin group (0.04 ± 0.01 vs. 0.19 ± 0.07,

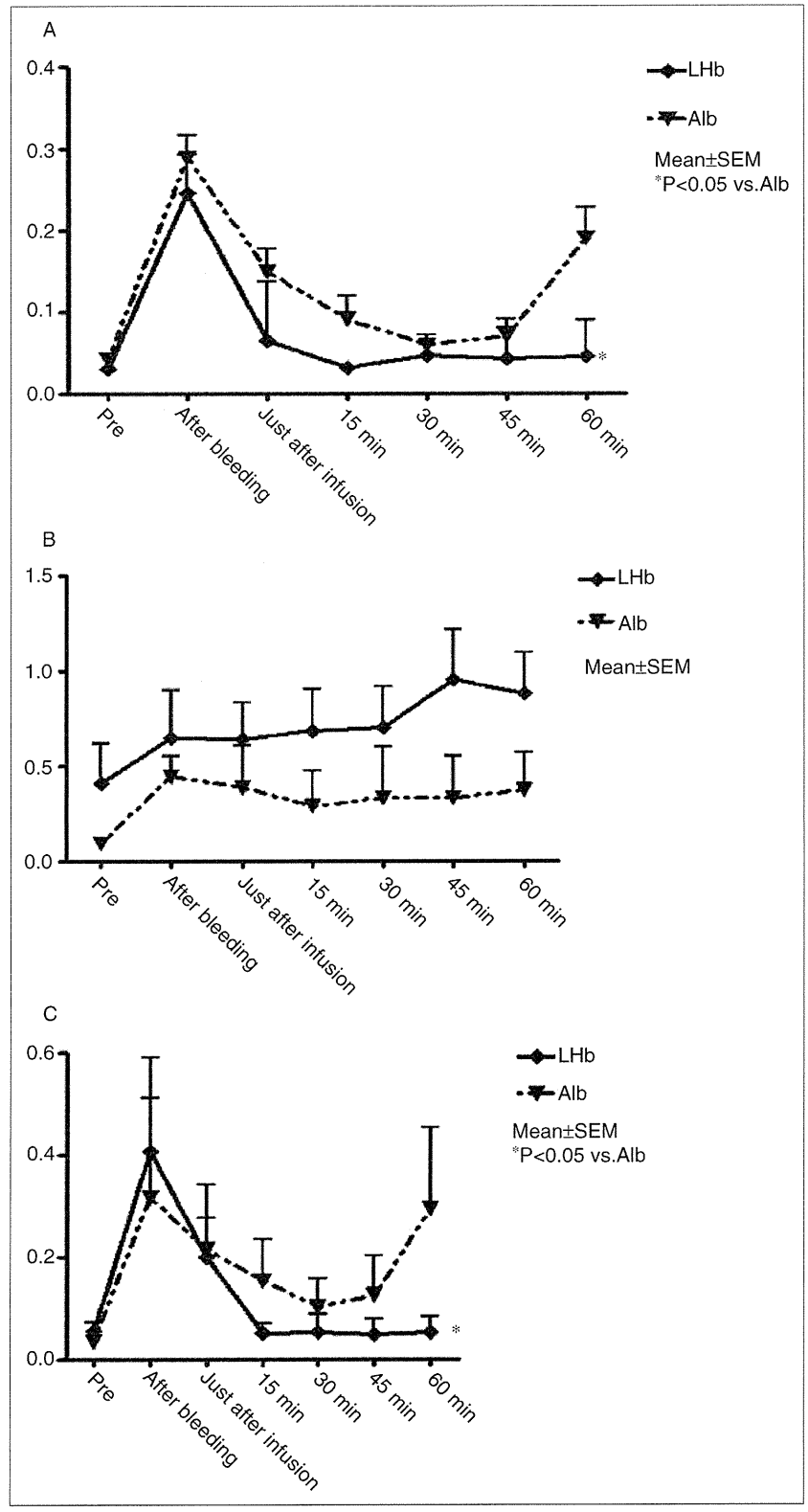


**Figure 5**
Temporal changes in low frequency spectra (LF, $ms^2/Hz$; panel **A**), high frequency spectra (HF, $ms^2/Hz$; panel **B**), and LF/HF ratio (panel **C**) in hemorrhagic shock resuscitated with either polyethylenglycol-modified liposome-encapsulated hemoglobin (LHb) or volume expander of 5% albumin. Format and abbreviations are identical to those in Figure 4.

$P < 0.05$; **Figure 5-A**). Values of the HF spectra tended to be higher in the LHb group when compared with the Albumin group at most time points, but this difference did not reach the level of statistical significance (**Figure 5-B**). The LF/HF ratio after resuscitation tended to be lower in the LHb

group than the Albumin groups (**Figure 5-C**). In addition, the LF/HF ratio at 60 min after resuscitation was significantly lower in the LHb than in the Albumin group ($0.05 \pm 0.01$ vs. $0.29 \pm 0.14$, $P < 0.05$).

## Discussion

The present study demonstrates that induction of hemorrhagic shock resulted in changes in autonomic nervous system activity, as evaluated by HRV. The LF spectra and LF/HF ratio increased during spontaneous recovery from hemorrhagic shock (Sham group), which is consistent with previous reports of augmented sympathetic nervous system activity in response to hemorrhagic shock.[1–6] Further, HRV changed during the recovery phase of hemorrhagic shock without concomitant changes in heart rate, which suggests that heart rate alone is not a suitable proxy for sympathetic nervous system activity, specifically, in the setting of 20% hemorrhagic shock recovery phase.

The changes in LF and LF/HF ratio in the Sham group over the time period of the study also suggest that these observations are the natural course of HRV indices during the sublethal hemorrhage. The marked increase in the LF and LF/HF ratio immediately after bleeding indicates the presence of a compensatory sympathetic surge in response to prompt bleeding and cardiovascular collapse. Subsequent and transient decrease in the LF and LF/HF ratio took place due to stoppage of bleeding. Finally, gradual increases of LF and LF/HF ratio have continued over the recovery phase of bleeding compensating for blood loss in order to maintain blood pressure.

In general, HRV reflects sympathetic nervous system or vagal activity.[7,8] However, confounding factors, such as respiration and/or anesthesia, may alter the relationship between HRV and autonomic nervous system activity. In this study, LF spectra and LF/HF ratio changed during the recovery phase of hemorrhagic shock despite use of general anesthesia with spontaneous breathing. Thus, the power spectral technique for measurement of HRV appears to be a useful technique to assess changes in autonomic nervous system activity during hemorrhagic shock under general anesthesia without control respiration.

In addition, several compensatory responses including both neural and humoral responses take place after the significant hemorrhagic shock. Among these mechanisms, following compensatory responses are considered (1) prompt increase in cardiac contraction with and without the modification of peripheral vascular tone through changing autonomic nervous activities, (2) humoral changes in order to preserve intravascular volume and salt, and (3) changes in the regional microcirculation to regulate organ blood perfusion. These phenomena were mainly caused by two pathways; one is autonomic nervous system and another is hypothalamic-pituitary adrenal axis. These systems are significantly activated after hemorrhagic shock.[20] The relation between autonomic nervous system and HRV indices has already been discussed earlier. In the hypothalamic-pituitary adrenal axis, compensatory activity of the rennin-angiotensin system occurs after hemorrhagic shock. Among HRV indices, LF has been influenced by rennin-angiotensin system and the value of LF increase in accordance with rennin-angiotensin system activation.[21] Our observation of compensatory increase of LF after hemorrhagic shock in Sham and Saline groups (**Figure 3**) agrees with the earlier report.

According to a well-accepted concept,[20] heart rate and HRV are physiologically correlated with each other. However, this correlation could deteriorate in the case of the alteration or collapse of cardiovascular system as occurs during hemorrhagic shock. The dissociation of heart rate and HRV immediately after bleeding in this study can be explained by the impairment of the harmonic relationship between heart rate and HRV due to cardiovascular collapse. The large values of LF and LF/HF ratio despite bradycardia immediately after bleeding suggest that the heart and vessels could not respond properly to the sympathetic drive. After the treatments or even with no treatment (Sham group), the heart and vascular system could begin to gradually respond to the sympathetic drive.

Many previous reports indicate that acute bleedings of 20% of total body blood causes significant hypotension up to the level of hemorrhagic shock. According to the previous reports,[23–27] a moderate amount of rapid bleeding (ranging from 17% to 30%) can cause reversible hemorrhage shock that is similar to the condition observed in this study. In addition, as pointed out by Secher et al,[23] the relative bradycardia can occur during hemorrhage[23,24] while tachycardia is considered as the typical feature for acute hemorrhage. Transient and reversible hypotension as well as relative bradycardia observed in this study are in agreement with these reports.

Experimental findings from the present study are consistent with those from past studies. For example, previous studies have reported that the LF spectra increased in response to hemorrhagic shock, whereas

there was no consistent change in the HF spectra.[24] In contrast, another study reported that the HF spectra decreased in response to acute blood loss, which suggests decreased vagal activity.[28] Finally, another group recently reported that the HRV is a good indicator of the change in autonomic nervous system activity during hemorrhage.[29] In this report, central volume in the body is well reflected the changes in the HRV indices.

The present study demonstrated that treatment with LHb as well as SAB significantly attenuated sympathetic nervous system activity during the recovery phase of hemorrhagic shock. Indeed, the LF spectra and LF/HF ratio during the recovery phase of hemorrhagic shock were significantly lower in the LHb and SAB groups than in the Saline and Sham groups. In addition, HF spectra tended to be higher in the LHb group when compared with the Sham, SAB and Albumin groups. These observations are consistent with conventional knowledge regarding the physiology of hemorrhagic shock. For example, increases in vagal activity can counteract the hemodynamic changes associated with hemorrhagic shock,[30–33] and increases in vagal activity and decreases in sympathetic nervous system activity occur during the recovery from hemorrhagic shock.[6,34]

The LF spectra and LF/HF ratio during the recovery phase of hemorrhagic shock were significantly lower in the LHb group than in the Albumin group. These observations suggest that volume expander of 5% albumin alone could not attenuate sympathetic nervous system activity during the recovery phase of hemorrhagic shock. Similar to SAB, LHb might have a volume-expansive effect. However, our results showed that volume expansion alone did not attenuate sympathetic nervous system activity so we presume that the oxygen carrying capacity of LHb could cause attenuation of sympathetic nervous system activity during the recovery phase of hemorrhagic shock.

LHb has excellent oxygen-carrying capacity, and its particle diameter is only 220 nm (nearly 30 times smaller than a human red blood cell[2]), allowing it to easily penetrate into the microcirculation, even during hemorrhagic shock which may induce vasoconstriction. These characteristics allow improved oxygen delivery to tissues and may also LHb to modulate autonomic control of the heart during hemorrhagic shock via its direct effects on circulation and its ability to inhibit chemo-reflex sensitivity. Further study of the mechanisms by which LHb modulates autonomic nervous system activity during hemorrhagic shock would be of benefit.

Study limitations: This study has several limitations. We did not give liposome with the same structure without oxygen carrying capacity to the hemorrhagic shock rats. To clarify whether liposomal capsules have volume-expansive effect and induce elevation of blood pressure, and then modulate autonomic nervous system activity during hemorrhagic shock, liposomal capsules with the same structure without oxygen carrying capacity should be studied in the future. Lastly, we only used the MemCalc system to measure HRV indices that is modified maximum entropy method. We presume that either Fast fourier transform or complex demodulation method can be applied to our experimental model.

Acknowledgements

We thank Dr. Y. Morimoto and Dr. M. Ishihara (Department of Medical Engineering, National Defense Medical College) for helpful discussions regarding the experimental procedure, and Dr. N. Matsutani, Dr. S. Isoda, Dr. M. Shimizu, Dr. T. Kimura, Dr. T. Nakayama, and Dr. S. Nakamura (Department of Surgery, National Defense Medical College) for helpful discussions regarding the experiment results.

## References

1) Carneiro JJ, Donald DE: Blood reservoir function of dog spleen, liver, and intestine. Am J Physiol 1977; 232: H67–72
2) Koyama S, Aibiki M, Kanai K, Fujita T, Miyakawa K: Role of central nervous system in renal nerve activity during prolonged hemorrhagic shock in dogs. Am J Physiol 1988; 254: R761–69
3) Koyama S, Sawano F, Matsuda Y, Saeki Y, Shibamoto T, Hayashi T, Jr., Matsubayashi Y, Kawamoto M: Spatial and temporal differing control of sympathetic activities during hemorrhage. Am J Physiol 1992; 262: R579–585
4) Schmidt HB, Werdan K, Muller-Werdan U: Autonomic dysfunction in the ICU patient. Curr Opin Crit Care 2001; 7: 314–322
5) Jacobsen J, Secher NH: Heart rate during haemorrhagic shock. Clin Physiol 1992; 12: 659–666
6) Sander-Jensen K, Secher NH, Bie P, Warberg J, Schwartz TW: Vagal slowing of the heart during haemorrhage: observations from 20 consecutive hypotensive patients. Br Med J (Clin Res Ed) 1986; 292: 364–366
7) Lombardi F, Malliani A, Pagani M, Cerutti S: Heart rate variability and its sympatho-vagal modulation. Cardiovasc Res 1996; 32: 208–216
8) Akselrod S, Gordon D, Ubel FA, Shannon DC, Berger AC, Cohen RJ: Power spectrum analysis of heart rate fluctuation: a quantitative probe of beat-to-beat cardiovascular control. Science 1981; 213: 220–222
9) Gould SA, Moore EE, Hoyt DB, Burch JM, Haenel JB, Garcia J, DeWoskin R, Moss GS: The first randomized trial of human polymerized hemoglobin as a blood substitute in acute trauma and emergent surgery. J Am

Coll Surg 1998; 187: 113–20; discussion 120–122
10) Moore EE, Cheng AM, Moore HB, Masuno T, Johnson JL: Hemoglobin-based oxygen carriers in trauma care: scientific rationale for the US multicenter prehospital trial. World J Surg 2006; 30: 1247–1257
11) Bjorkholm M, Fagrell B, Przybelski R, Winslow N, Young M, Winslow RM: A phase I single blind clinical trial of a new oxygen transport agent (MP4), human hemoglobin modified with maleimide-activated polyethylene glycol. Haematologica 2005; 90: 505–515
12) Doherty DH, Doyle MP, Curry SR, Vali RJ, Fattor TJ, Olson JS, Lemon DD: Rate of reaction with nitric oxide determines the hypertensive effect of cell-free hemoglobin. Nat Biotechnol 1998; 16: 672–676
13) Schultz SC, Grady B, Cole F, Hamilton I, Burhop K, Malcolm DS: A role for endothelin and nitric oxide in the pressor response to diaspirin cross-linked hemoglobin. J Lab Clin Med 1993; 122: 301–308
14) Ogata Y, Goto H, Kimura T, Fukui H: Development of neo red cells (NRC) with the enzymatic reduction system of methemoglobin. Artif Cells Blood Substit Immobil Biotechnol 1997; 25: 417–427
15) Nakai K, Usuba A, Ohta T, Kuwabara M, Nakazato Y, Motoki R, Takahashi TA: Coronary vascular bed perfusion with a polyethylene glycol-modified hemoglobin-encapsulated liposome, neo red cell, in rats. Artif Organs 1998; 22: 320–325
16) Sakai H, Masada Y, Horinouchi H, Yamamoto M, Ikeda E, Takeoka S, Kobayashi K, Tsuchida E: Hemoglobin-vesicles suspended in recombinant human serum albumin for resuscitation from hemorrhagic shock in anesthetized rats. Crit Care Med 2004; 32: 539–545
17) Sakai H, Takeoka S, Wettstein R, Tsai AG, Intaglietta M, Tsuchida E: Systemic and microvascular responses to hemorrhagic shock and resuscitation with Hb vesicles. Am J Physiol Heart Circ Physiol 2002; 283: H1191–1199
18) Oda T, Kimura T, Ogata Y, Fujise Y: Hemodilution with liposome-encapsulated low-oxygen-affinity hemoglobin does not attenuate hypothermic cerebral ischemia in rats. J Artif Organs 2005; 8: 263–269
19) Nogami Y, Takase B, Matsui T, Hattori H, Hamabe A, Fujita M, Ohsuzu F, Ishihara M, Maekara T: Effect of antiarrhythmic agents on heart rate variability indices after myocardial infarction: comparative experimental study of aprindine and procainamide. Biomed Pharmacother 2005; 59 Suppl 1: S169–173
20) Peitzman AB, Harbrecht BG, Billar TR: Shock. In Brunicardi FC ed: Schwartz's Principles of Surgery. eighth edition., The McGraw-Hill Companies, Inc., USA, 2005, p85–107
21) Duprez DA, De Sutter JH, De Buyzere ML, Rietzschel ER, Rimbaut S, Kaufman JM, Van Hoecke MJ, Clement DL: Renin-angiotensin-aldosterone system, RR interval, and blood pressure variability during postural changes in borderline arterial hypertension. Am J Hypertens 1995; 8: 683–688
22) Coumel P, Maison-Blanche P, Catuli D: Heart rate and heart rate variability. In: Malik M, ed. Heart Rate Variability 1st ed. New York, Futura Publishing Company Inc., 1995, p207–222
23) Secher NH, Jacobsen J, Friedman DB, Matzen S: Bradycardia during reversible hypovolaemic shock: associated neural reflex mechanisms and clinical implications. Clin Exp Pharmacol Physiol 1992; 19: 733–743
24) Kawase M, Komatsu T, Nishiwaki K, Kimura T, Fujiwara Y, Takahashi T, Shimada Y: Heart rate variability during massive hemorrhage and progressive hemorrhagic shock in dogs. Can J Anaesth 2000; 47: 807–814
25) Tanaka T, Sato H, Kita T, Tanaka N: Involvement of inducible nitric oxide synthase in renal failure after mild hemorrhage. Leg Med (Tokyo) 2004; 6: 203–212
26) Bassin R, Vladeck BC, Kark AE, Shoemaker WC: Rapid and slow hemorrhage in man. I. Sequential hemodynamic responses. Ann Surg 1971; 173: 325–330
27) Monson DO, Shoemaker WC: Sequence of hemodynamic events after various types of hemorrhage. Surgery 1968; 63: 738–749
28) Zollei E, Paprika D, Makra P, Gingl Z, Vezendi K, Rudas L: Human autonomic responses to blood donation Auton Neurosci 2004; 110: 114–120
29) Cooke WH, Convertino VA: Heart rate variability and spontaneous baroreflex sequences: implications for autonomic monitoring during hemorrhage. J Trauma 2005; 58: 798–805
30) Vergoni AV, Marrama D, Guarini S, Tagliavini S, Bazzani C, Maugeri A, Bertolini A: Afferent vagal fibres and central cholinergic mechanisms are involved in the TRH-induced reversal of haemorrhagic shock. Pharmacol Res 1991; 23: 271–278
31) Guarini S, Altavilla D, Cainazzo MM, Giuliani D, Bigiani A, Marini H, Squadrito G, Minutoli L, Bertolini A, Marini R, Adamo EB, Venuti FS, Squadrito F: Efferent vagal fibre stimulation blunts nuclear factor-kappaB activation and protects against hypovolemic hemorrhagic shock. Circulation 2003; 107: 1189–1194
32) Velasco IT, Baena RC: The role of the vagus nerve in hypertonic resuscitation of hemorrhagic shocked dogs. Braz J Med Biol Res 2004; 37: 419–425
33) Schertel ER, Valentine AK, Schmall LM, Allen DA, Muir WW: Vagotomy alters the hemodynamic response of dogs in hemorrhagic shock. Circ Shock 1991; 34: 393–397
34) Lopes OU, Pontieri V, Rocha e Silva M, Jr., Velasco IT: Hyperosmotic NaCl and severe hemorrhagic shock: role of the innervated lung. Am J Physiol 1981; 241: H883–890

THE JOURNAL OF BIOLOGICAL CHEMISTRY VOL. 285, NO. 49, pp. 38428–38437, December 3, 2010


# Structural Requirements for Activation in αIIbβ3 Integrin*[S]

Received for publication, April 30, 2010, and in revised form, September 17, 2010 Published, JBC Papers in Press, September 29, 2010, DOI 10.1074/jbc.M110.139667

**Tetsuji Kamata[‡1], Makoto Handa[§], Sonomi Ito[‡], Yukiko Sato[‡], Toshimitsu Ohtani[‡], Yohko Kawai[¶], Yasuo Ikeda[‖], and Sadakazu Aiso[‡]**

*From the Departments of [‡]Anatomy and [§]Transfusion Medicine and Cell Therapy, Keio University School of Medicine, 35 Shinanomachi, Shinjuku-ku, Tokyo 160-8582, the [¶]Preventive Health Examination Center, International University of Health and Welfare, 8-10-16 Akasaka, Minato-ku, Tokyo 107-0052, and the [‖]Department of Life Science and Medical Bio-Science, School of Advanced Science and Engineering, Waseda University, 2-2 Wakamatsu-cho, Shinjuku-ku, Tokyo 162-8480, Japan*

**Integrins are postulated to undergo structural rearrangement from a low affinity bent conformer to a high affinity extended conformer upon activation. However, some reports have shown that a bent conformer is capable of binding a ligand, whereas another report has shown that integrin extension does not absolutely lead to activation. To clarify whether integrin affinity is indeed regulated by the so-called switchblade-like movement, we have engineered a series of mutant αIIbβ3 integrins that are constrained specifically in either a bent or an extended conformation. These mutant αIIbβ3 integrins were expressed in mammalian cells, and fibrinogen binding to these cells was examined. The bent integrins were created through the introduction of artificial disulfide bridges in the β-head/β-tail interface. Cells expressing bent integrins all failed to bind fibrinogen unless pretreated with DTT to disrupt the disulfide bridges. The extended integrins were created by introducing *N*-glycosylation sites in amino acid residues located close to the α-genu, where the integrin legs fold backward. Among these mutants, activation was maximized in one integrin with an *N*-glycosylation site located behind the α-genu. This extension-induced activation was completely blocked when the swing-out of the hybrid domain was prevented. These results suggest that the bent and extended conformers represent low affinity and high affinity conformers, respectively, and that extension-induced activation depends on the swing-out of the hybrid domain. Taken together, these results are consistent with the current hypothesis that integrin affinity is regulated by the switchblade-like movement of the integrin legs.**

Integrin-mediated bidirectional signaling is closely associated with the structural rearrangement of integrin itself. During inside-out signaling, talin has been shown to bind to the β cytoplasmic tail and to disrupt the endogenous interaction between the α and β cytoplasmic tails (1, 2). The dissociation of the two tails induces a structural rearrangement of the extracellular domains increasing the affinity to the ligand. During outside-in signaling, ligand binding in turn induces the structural rearrangement of the extracellular domains. This structural change propagates through the plasma membrane to separate the cytoplasmic tails, providing binding sites for numerous cytoplasmic proteins (3). Thus, the two structures flanking the plasma membrane affect each other. This structural rearrangement can be detected using a group of monoclonal antibodies (mAbs) that bind preferentially to the ligand-bound form (4). These anti-LIBS[2] (ligand-induced binding site) mAbs have been used not only to investigate the activation status of a specific integrin but also to activate it (5). However, without information on the actual three-dimensional structure, it is impossible to determine the specific conformation recognized by each anti-LIBS mAb.

The first observation of the actual three-dimensional structure of integrin was made using conventional electron microscopy (EM) studies of αIIbβ3 purified from platelets (6, 7). Although this modality had a relatively low resolution, αIIbβ3 was shown to consist of a globular head with two short legs extending outward. A crystal structure analysis of the extracellular domains of αVβ3 integrin (PDB 1M1X) revealed that the α-chain consists of the N-terminal β-propeller domain followed by the thigh, calf-1, and calf-2 domains, whereas the β-chain consists of the plexin-semaphorin-integrin domain, βA domain, hybrid domain, four EGF domains, and βT domain (8). The β-propeller and βA domains non-covalently associate with each other to form the globular head that was observed in the EM images. In contrast, the thigh, calf-1, and calf-2 domains of the α-chain and the plexin-semaphorin-integrin, EGF, and βT domains of the β-chain form the two leg-like regions, respectively. Thus, the crystal structure is consistent with the conventional EM image described above. However, a striking difference in the orientation of the head was noted. In the crystal structure, the two legs were folded backward, with a 135° angle between the thigh and the calf-1 domains, unlike the straight legs observed using conventional EM. Consequently, the head region pointed downward, facing the plasma membrane. The discrepancies between these two structures were reconciled using high resolution EM images of the extracellular domains of recombinant αVβ3 integrin (9). This modality revealed that αVβ3 could adopt multiple distinct structures,

* This work was supported in part by Labor Sciences research grants (Research on Public Essential Drugs and Medical Devices) from the Ministry of Health, Labour and Welfare (to T. K. and M. H.), a grant from the Fukuzawa Memorial Foundation (to T. K.), and a grant-in-aid for scientific research (KAKENHI) from the Ministry of Education, Culture, Sports, Science and Technology (to S. A.).

[S] The on-line version of this article (available at http://www.jbc.org) contains supplemental Figs. S1–S3.

[1] To whom correspondence should be addressed: Dept. of Anatomy 3S1, Keio University School of Medicine, 35 Shinanomachi, Shinjuku-ku, Tokyo 160-8582. Japan. Tel.: 81-3-3353-1211, Ext. 63571; Fax: 81-3-5360-1524; E-mail: kamata@sc.itc.keio.ac.jp.

[2] The abbreviations used are: LIBS, ligand-induced binding site; Fbg, fibrinogen; TEV, tobacco etching virus.

including the bent and extended conformers observed in the crystal structure analysis and the conventional EM study, respectively. Because $Mn^{2+}$ and a ligand peptide significantly increased the number of extended forms, the extended form was suggested to represent a high affinity state, whereas the bent form was thought to represent a low affinity state. Thus, the transition from one conformer to another (or the so-called switchblade-like movement) might regulate the affinity of integrin to its ligand. Aside from this movement, substantial structural rearrangement has been observed in the head region (10). A crystal structure analysis of the αIIbβ3 head region when the molecule forms a complex with ligand mimetics revealed that the β-hybrid domain swings outward upon ligand binding (11). This movement is accompanied by the rearrangement of the ligand- and/or cation-binding loops in the βA domain, thereby regulating ligand binding (11).

However, contradictory reports suggest that integrin extension is not an essential event for ligand binding. Cryo-electron microscopic observations of αIIbβ3 purified from activated platelets revealed that this molecule adopts a rather compact structure, unlike the extended conformer (12). The crystal structure of αVβ3 complexed with a small peptide ligand revealed that the bent conformer was capable of binding a ligand (13). In this experiment, αVβ3 was understandably unable to undergo gross structural rearrangement upon ligand binding because of the constraints of the crystal lattice. However, a single particle analysis of recombinant αVβ3 complexed with a fibronectin fragment has shown that αVβ3 can bind macromolecular ligands while in a bent conformation in the presence of $Mn^{2+}$ (14, 15). This evidence suggests that the bent conformer is capable of binding both small ligands and macromolecular ligands without requiring substantial structural rearrangements.

In this study, we examined the relationship between the three-dimensional structure of integrin and its ligand affinity. Our findings provide evidence that the extended conformer represents a highly activated state, whereas the bent conformer represents a low affinity state. These results are consistent with the view that the ligand binding activity of integrin can be regulated allosterically through the switchblade-like movement of the legs of integrin, centering on the genu region.

## EXPERIMENTAL PROCEDURES

*Antibodies and Reagents*—Normal mouse IgG was purchased from Sigma-Aldrich. Anti-αIIb mAb PL98DF6 (16) was a generous gift from Drs. J. Ylänne (University of Oulu, Finland) and I. Virtanen (University of Helsinki, Finland). Anti-β3 mAbs anti-LIBS2 and anti-LIBS6 (17) were generous gifts from Dr. Mark H. Ginsberg (University of California, San Diego, La Jolla, CA). Anti-αIIbβ3 complex-specific ligand-mimetic mAb OP-G2 (18) was a kind gift from Dr. Yoshiaki Tomiyama (University of Osaka, Japan). Anti-αIIbβ3 complex-specific function-blocking mAb A2A9 was purchased from Santa Cruz Biotechnology (Santa Cruz, CA). Anti-αIIbβ3 complex-specific activating mAb PT25-2 and non-functional anti-β3 mAb VNR5-2 have previously been characterized (19). Anti-β3 mAb SZ21 was purchased from Beckman Coulter. Anti-FLAG mAb M2 was purchased from Sigma-Aldrich. R-Phycoerythrin-conjugated goat anti-mouse polyclonal antibody was purchased from BIOSOURCE (Camarillo, CA). Synthetic peptide Gly-Arg-Gly-Asp-Ser (GRGDS) was purchased from Peptide Research Institute (Osaka, Japan). Fluorescein-isothiocyanate (FITC) was purchased from Sigma-Aldrich. Human fibrinogen (Fbg) was purchased from Enzyme Research Laboratories (South Bend, IN). The tobacco etching virus (TEV) protease TurboTEV protease and peptide *N*-glycosidase F were purchased from Accelagen (San Diego, CA) and New England Biolabs (Ipswich, MA), respectively.

*Construction of Mutant αIIb and β3 cDNA Clones*—The full-length cDNAs for the integrin αIIb and β3 subunits, generous gifts from Dr. Joseph C. Loftus (Mayo Clinic, Scottsdale, AZ), were cloned into the mammalian expression vector pBJ-1, kindly provided by Dr. Mark Davis (University of California, San Francisco). The cDNAs for the β3 mutants V332C, S367C, G382C, S551C, T564C, S674C, S367C/S551C, G382C/T564C, V332C/S674C, V332N, S674N/K676T, V332N/S674N/K676T, and V359C and the cDNAs for the αIIb mutants T478N, D589N/H591T, Q595N/R597T, Q595A/R597T, Q595W/R597T, Q595D/R597T, Q595N, R597T, Q595N/R597A, Q595N/R597S, D319C, and Q595N/R597T/D319C were created using the Transformer site-directed mutagenesis kit (BD Biosciences). The cDNAs for β3 del 671–676 (del-CD) and β3 FLAG 671–676 (FLAG-CD) were also created using site-directed mutagenesis and 5′-GATTCCAGTACTATTCCATCCTGTATGTG-3′ and 5′-CAGATTCCAGTACTATTCCATCCTGTATG-3′ as mutagenic primers, respectively. The TEV protease recognition site Glu-Asn-Leu-Tyr-Phe-Gln-Gly was introduced to amino acid residues 475–481 of the β3 chain (475TEV) using 5′-GTGTGAGTGCTCAGAGAACCTCTATTTCCAAGGCCAGCAGGACGAATGCAGC-3′ as a mutagenic primer. Two additional mutations, C473S and C503S, were introduced in 475TEV using site-directed mutagenesis (475TEVCS). The S367C/S551C, G382C/T564C, or V332C/S674C double mutations were introduced in 475TEVCS utilizing common restriction sites. To create the cDNA for the FLAG-αIIb450 fragment, a FLAG tag sequence was inserted at the 5′ terminus of wild-type αIIb cDNA followed by a BstEII restriction site using 5′-GCTGCCCCTCCAGCCTGGGCCGACTACAAGGACGACGATGACAAGGGGTCACCATTGAACCTGGACCCAGTGCAGC-3′ as a mutagenic primer (FLAG-αIIb). Next, the BstEII restriction site was introduced at the 5′ side of Ala-450 using 5′-CCAGGTGGCTGGGTCACCAGCTCAGCCAGTG-3′ as a mutagenic primer (αIIbBstE450). Then, the cDNA for the FLAG-αIIb450 fragment was created by replacing the 5′-terminal BstEII/BglII fragment of FLAG-αIIb with the same fragment from αIIbBstE450. Finally, the cDNA for the FLAG-αIIb450 fragment carrying the T478N, D589N/H591T, Q595N/R597T, or R597T mutation was created by combining these mutations using common restriction sites.

*Cell Culture and Transfection*—Chinese hamster ovary (CHO)-K1 cells were cultured in Dulbecco's modified Eagle's medium (Invitrogen) supplemented with 10% fetal calf serum (HyClone, Logan, UT), 1% penicillin and streptomycin (Invitrogen), and 1% non-essential amino acids (Sigma-Aldrich) and maintained at 37 °C in a humidified incubator supplemented

with 5% $CO_2$. Fifty micrograms of αIIb cDNA construct was co-transfected with 50 μg of β3 cDNA construct into CHO-K1 cells using electroporation. After 48 h, the cells were detached and used for further experiments.

*Flow Cytometry*—Cells were detached with phosphate-buffered saline (PBS) containing 3.5 mM EDTA. After washing, the cells were incubated with 10 μg/ml mAb in modified HEPES-Tyrode's buffer (5 mM HEPES, 5 mM glucose, 0.2 mg/ml bovine serum albumin, 1× Tyrode's solution) supplemented with 1 mM $CaCl_2$ and 1 mM $MgCl_2$ for 30 min at 4 °C. In some experiments, 1 mM GRGDS peptide was included together with the mAbs. After washing, the cells were incubated with the R-Phycoerythrin-conjugated F(ab')2 fragment of goat anti-mouse IgG for 30 min at 4 °C. After washing, the cells were resuspended in HEPES-buffered saline (10 mM HEPES, 150 mM NaCl (pH 7.4)) containing 1 mM $CaCl_2$ and 1 mM $MgCl_2$. Fluorescence was measured using a FACSCalibur (BD Biosciences). To compare the binding of conformation-dependent mAbs among cells expressing different αIIbβ3 mutants, each mAb binding was normalized by the expression of αIIbβ3 on the cell surface. This relative mAb binding was calculated by dividing the mean fluorescent intensity obtained for each mAb by the mean fluorescent intensity obtained for the non-conformation-dependent anti-β3 mAb SZ21 or the anti-αIIbβ3 complex-specific mAb A2A9.

*Fibrinogen Binding Assay*—FITC labeling of human Fbg was performed as described previously (20). Briefly, after adjusting the pH of human Fbg at 1 mg/ml in PBS to 8.5 using 5% $Na_2CO_3$, 1/100 volume of 10 mg/ml FITC in dimethyl sulfoxide (DMSO) was added and incubated at room temperature for 10 min. FITC-labeled Fbg was separated from free FITC on a PD-10 column (Amersham Biosciences, Uppsala, Sweden) equilibrated with HEPES-buffered saline. The concentration and fluorescence-to-protein ratio of FITC-labeled Fbg were calculated as described previously. The typical concentration and fluorescence-to-protein ratio were 3.4 mg/ml and 5.0 – 6.0, respectively. Forty-eight hours after transfection, the cells were detached and washed once with HEPES-Tyrode's buffer. The αIIbβ3-transfected cells were incubated with non-functional anti-αIIb mAb PL98DF6 followed by incubation with the ribulose-phosphate 3-epimerase-conjugated F(ab')2 fragment of goat anti-mouse IgG. In some experiments, cells were treated with dithiothreitol (DTT) prior to incubation with the mAbs, as described previously (19). After washing, the cells were incubated with 340 μg/ml FITC-labeled Fbg with or without 1 mM GRGDS peptide in HEPES-Tyrode's buffer containing 1 mM $CaCl_2$ and 1 mM $MgCl_2$ or 1 mM $MnCl_2$ for 2 h at 4 °C. In some experiments, the mAb PT25-2 was included at a concentration of 10 μg/ml to activate αIIbβ3. After washing, fluorescence was measured using a FACSCalibur. The mean Fbg binding (FL1) to cell populations expressing high levels of αIIb (FL2 > 500) was calculated. Background binding in the presence of 1 mM GRGDS peptide was subtracted to obtain the specific binding.

*Immunoprecipitation*—Biotin labeling of the cell surface protein was done using Sulfo-NHS-Biotin (Thermo Scientific) following the manufacturer's instructions. Cells were lysed in 1 ml of lysis buffer (100 mM *n*-octylglucopyranoside, 20 mM *N*-ethyl maleimide, 1 mM PMSF, 25 mM Tris-HCl, and 150 mM NaCl, pH 7.4). After removing the insoluble material by centrifugation, the supernatant was used for further analysis. Two hundred microliters of cell lysate was precleared by adding 1 μg of mouse IgG, together with 20 μl of protein G-agarose beads. After centrifugation, the supernatant was recovered and further incubated with 1 μg of PL98DF6 or VNR5-2, together with 20 μl of protein G-agarose beads overnight at 4 °C. Then, the supernatant was discarded, and the remaining protein G-agarose beads were washed three times with washing buffer (25 mM Tris-HCl, 150 mM NaCl, 0.01% Triton X-100 (pH 8.0)). The protein G-agarose beads were resuspended in 10 μl of washing buffer. The TEV protease digestion of the immunoprecipitates was performed by adding 1 μl of TurboTEV to the suspension with or without 1 mM DTT followed by incubation for 3 h at 30 °C. The peptide *N*-glycosidase F digestion of the immunoprecipitates was done according to the manufacturer's instructions except that the DTT was excluded from the denaturation buffer. After digestion, the samples were subjected to 7.5 or 10% SDS-PAGE, transferred to a polyvinylidene difluoride membrane, probed with horseradish peroxidase-conjugated avidin, and detected using chemiluminescence with West Pico chemiluminescent substrate (Thermo Scientific).

## RESULTS

*Bent Conformer of αIIbβ3 Represents a Low Affinity Form*—In the αVβ3 crystal structure, in addition to the α-head and β-head, the β-head and β-tail domains create a large interface that keeps αVβ3 in a bent conformation (8, 13). To constrain αIIbβ3 in this bent conformation, artificial disulfide bridges were introduced at different locations in the β-head/β-tail interface. As shown in Fig. 1*A*, the amino acid residues Ser-367 and Gly-382 in the hybrid domain and Val-332 in the βA domain are localized close to Ser-551 in the EGF-3 domain, Thr-564 in the EGF-4 domain, and Ser-674 in the βT domain, respectively. If these residues are simultaneously mutated to Cys, a disulfide bride is expected to form. Thus, the resulting S367C/S551C, G382C/T564C, and V332C/S674C double mutations are expected to stabilize the hybrid/EGF-3, the hybrid/EGF-4, and the βA/βT interfaces, respectively. In either case, these mutations should prevent the β3 chain from adopting an extended conformation. These mutants were expressed in CHO cells, and FITC-labeled Fbg binding to these cells was examined using FACS. As reported previously, the wild-type αIIbβ3 expressed in CHO cells is in a low affinity state and requires activation by the anti-αIIbβ3 mAb PT25-2 to bind Fbg in the presence of 1 mM $Ca^{2+}$/1 mM $Mg^{2+}$ (20). Cells expressing single Cys mutations, such as S367C, G382C, V332C, S551C, T564C, or S674C, bound Fbg in the presence of PT25-2, albeit slightly less than that observed in wild-type cells (data not shown). By contrast, cells expressing double Cys mutations were completely unable to bind Fbg unless they were pretreated with DTT to disrupt the disulfide bridges (Fig. 1*B*). These artificially introduced disulfides did not affect PT25-2 binding to αIIbβ3 (supplemental Fig. S1). These results suggest that the blocking effect of the double mutation is actually caused by disulfide bridge formation between the mutated residues, rather than a local effect of the mutation itself.

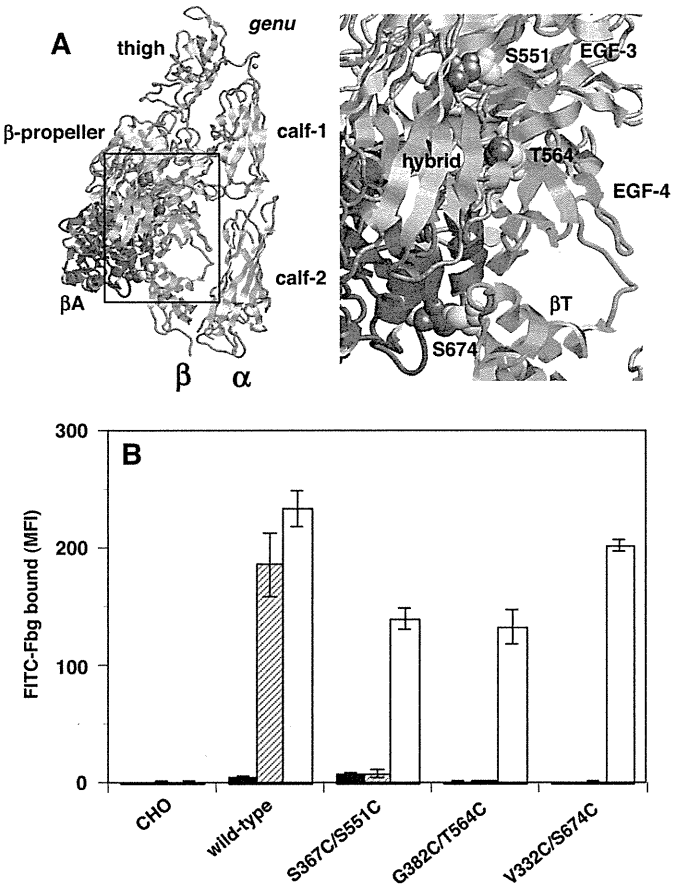


FIGURE 1. **Effect of β-head/β-tail interface stabilization on the αIIbβ3-Fbg interaction.** *A*, crystal structure of the αVβ3 integrin. The entire αV chain is shown as the *gray ribbon*. The βA and hybrid domains that compose the head region of the β3 chain are shown as *red* and *orange ribbons*, respectively. The EGF-3, EGF-4, and βT domains that compose the β-tail of the β3 chain are shown as the *green ribbon*. The β-head/β-tail interface shown in the rectangle is magnified in the *right-hand panel*. Amino acid residues Ser-367 and Gly-382 in the hybrid domain and Val-332 in the βA domain are shown as *magenta spacefill*. These residues are closely located to Ser-551 in the EGF-3 domain, Thr-564 in the EGF-4 domain, and Ser-674 in the βT domain, respectively, which are shown as *yellow spacefill*. Only the residues in the β-tail are labeled. To constrain αIIbβ3 in its bent conformation, these four residue couples were simultaneously mutated to Cys to facilitate disulfide bridge formation. *B*, Fbg binding to cells expressing αIIbβ3 constrained in the bent conformation in the presence of 1 mM $Ca^{2+}$/1 mM $Mg^{2+}$ and control antibody (*solid column*), in the presence of 1 mM $Ca^{2+}$/1 mM $Mg^{2+}$ and PT25-2 (*hatched column*), and in cells pretreated with DTT in the presence of 1 mM $Ca^{2+}$/1 mM $Mg^{2+}$ (*open column*) is shown. *MFI*, mean fluorescent intensity. *Error bars* indicate S.E.

To examine whether these artificially introduced disulfide bridges stabilize the β-head/β-tail interface, we introduced a TEV protease recognition site between the head and tail regions of the β3 chain (21). This mutation (475TEV) was designed to separate the N-terminal head region (amino acids 1–480) from the C-terminal tail region (amino acids 481–762) of the β3 chain upon TEV protease digestion. Because these two regions are connected by a disulfide bridge formed by Cys-473 and Cys-503, these residues were mutated to Ser (475TEVCS) to facilitate separation upon digestion. Then, we introduced S367C/S551C, G382C/T564C, and V332C/S674C double mutations in 475TEVCS. These mutant β3 chains were expressed together with wild-type αIIb in CHO cells. The surface-expressed β3 was immunoprecipitated with anti-β3 mAb and analyzed using SDS-PAGE. All the mutant β3 chains co-precipitated with αIIb, as did wild-type β3, with the exception that a slight difference in the electrophoretic mobility of the mutant β3 chains was noted (supplemental Fig. S2*A*). When digested with TEV protease under non-reducing conditions, only 475TEVCS generated a 70-kDa band in place of a 98-kDa intact β3 chain (supplemental Fig. S2*B*). However, all but the wild-type β3 generated 73- and 43-kDa bands in place of a 116-kDa band when digested with TEV protease under reducing conditions (supplemental Fig. S2*C*). The results indicate that 475TEVCS is indeed cleaved into a 73-kDa N-terminal head region and a 43-kDa C-terminal tail region by TEV protease, as expected. Because these two regions are still connected by a disulfide bridge in 475TEVCS 367/551, 475TEVCS 382/564, and 475TEVCS 332/674 as well as in 475TEV, the two fragments could not separate from each other under non-reducing conditions, although β3 was already cleaved by the TEV protease treatment. However, under reducing conditions, these mutant β3 molecules readily separated into two fragments. These results prove that in S367C/S551C, G382C/T564C, and V332C/S674C mutants, the disulfide bridge actually ligates the head and the tail regions of the β3 chain, thereby stabilizing the β-head/β-tail interface.

*βA/βT Interface Interaction Is Not Sufficient to Act as a Deadbolt to Maintain Integrin in a Low Affinity State*—Xiong *et al.* (8) initially reported that the βA/βT interface interaction might act as a deadbolt to keep integrin in a low affinity state by preventing the movement of the α7 helix of βA, which is associated with ligand binding. Indeed, stabilizing this interface with a disulfide bridge (V332C/S674C) completely inhibited ligand binding (Fig. 1*B*). To further examine this hypothesis, amino acid residues 671–676 of β3, composing most of the CD loop (Fig. 2*A*) that participates in βA/βT interface formation, was either deleted (del-CD) or replaced with an irrelevant FLAG tag sequence (FLAG-CD). When expressed in CHO cells, the del-CD or FLAG-CD mutant did not bind Fbg unless activated by PT25-2 in the presence of $Ca^{2+}$/$Mg^{2+}$. One mM $Mn^{2+}$ did not significantly increase Fbg binding in del-CD, as it did in wild-type cells. However, cells expressing the FLAG-CD mutant bound ~2.5 times as much Fbg as cells expressing wild-type αIIbβ3 (Fig. 2*B*). These results suggest that although the endogenous βA/CD loop interface interaction alone does not play a critical role in constraining αIIbβ3 in a low affinity state, alterations in its interactions might affect the activation status. The FLAG tag sequence (DYKDDDDK) consists of 8 amino acid residues when compared with the 6 residues in the wild-type sequence. This may imply that physical separation of the two domains can induce activation. To induce complete separation, we attempted to insert a bulky spacer between the βA and the βT domains. This would not only disrupt the βA/βT interface interaction completely but would also affect the hybrid/βT interface formation and slightly extend the integrin. For this purpose, we created an *N*-linked glycosylation site (N*X*(T/S) motif) at Val-332 and/or Ser-674 in the interface (Fig. 2*A*). When the 332VLS[3] sequence in the βA was mutated to

[3] 332VLS and 674SGK designate wild-type β3 sequences. The three letters following the number represent the amino acid residues starting from the position the number represents.

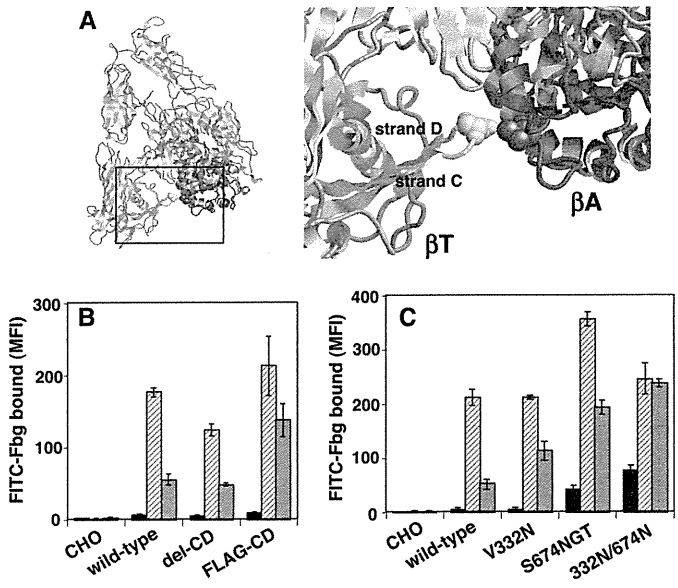


FIGURE 2. **Role of the βA/CD loop interaction in αIIbβ3 activation.** *A*, the βA and βT domains are shown as *red* and *green ribbons*, respectively. The βA/CD loop interface shown in the *rectangle* is magnified on the *right-hand side*. Amino acid residues 671–676 in the β3 domain that contain the CD loop in the βT domain are shown in *yellow*. Val-332 in the βA domain and Ser-674 in the CD loop are shown as *magenta* and *yellow spacefill*, respectively. *B*, the CD loop sequences were either deleted (del-CD) or replaced with an irrelevant FLAG tag sequence (FLAG-CD). *MFI*, mean fluorescent intensity. *C*, bulky *N*-glycan-binding sites were introduced either at Val-332 (V332N) or at Ser-674 (S674N/K676T), or in combination (332N/674N). Fbg binding to the cells in the presence of 1 mM $Ca^{2+}$/1 mM $Mg^{2+}$ and a control antibody and in the presence of 1 mM $Ca^{2+}$/1 mM $Mg^{2+}$ and PT25-2 is shown as the *solid* and *hatched columns*, respectively. Fbg binding in the presence of 1 mM $Mn^{2+}$ with control antibody is shown as the *gray column*. *Error bars* indicate S.E.

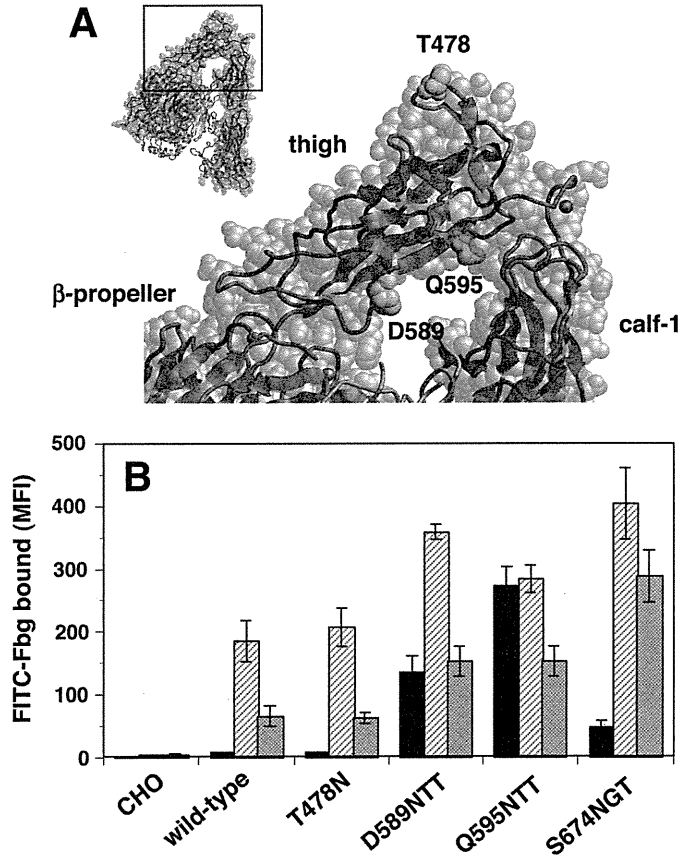


FIGURE 3. **Effect of integrin extension on ligand binding.** *A*, the three-dimensional structure of the αV chain is shown as *semitransparent blue spacefill* with its backbone as a *blue ribbon*. The β3 chain is shown as a *gray ribbon*. Structures around α-genu in the rectangle are magnified below. The positions of the amino acid residues Thr-466, Pro-583, and Gln-589, which are homologous to Thr-478, Asp-589, and Gln-595 in αIIb, are shown as *cyan spacefill* and labeled as such. Note that Gln-595 is located immediately behind the genu. *B*, an *N*-glycosylation site was introduced at Thr-478, Asp-589, and Gln-595 in the αIIb chain or at Ser-674 in the β3 chain. The resulting αIIbβ3 mutants T478N, D589N/H591T, Q595N/R597T, and S674N/K676T were expressed in CHO cells. Fbg binding to cells in the presence of 1 mM $Ca^{2+}$/1 mM $Mg^{2+}$ and control antibody and in the presence of 1 mM $Ca^{2+}$/1 mM $Mg^{2+}$ and PT25-2 is shown as the *solid column* and *hatched columns*, respectively. Fbg binding in the presence of 1 mM $Mn^{2+}$ with control antibody is shown as the *gray column*. *MFI*, mean fluorescent intensity. *Error bars* indicate S.E.

332NLS (V332N), it did not have any effect on Fbg binding in the presence of $Ca^{2+}/Mg^{2+}$. However, cells expressing the V332N mutant bound approximately twice as much Fbg as cells expressing the wild-type in the presence of $Mn^{2+}$. When the 674SGK sequence was mutated to 674NGT (S674N/K676T), slight but consistent Fbg binding was observed in the presence of $Ca^{2+}/Mg^{2+}$ without any activators. The addition of PT25-2 or $Mn^{2+}$ induced more robust Fbg binding than the wild type. Combining these two mutations (V332N/S674N/K676T) had a synergistic effect on constitutive binding, although it did not further increase binding in the presence of $Mn^{2+}$ (Fig. 2*C*). These results suggest that the more the βA and βT domains are separated, the stronger the activation of αIIbβ3. In other words, integrin extension by itself may induce activation.

*Extended Conformer of αIIbβ3 Represents a Highly Activated Form*—The βA domain provides a part of the ligand-binding site. Therefore, any direct change imposed on the βA domain might affect ligand binding. To induce integrin extension without directly affecting the ligand-binding domains, we introduced *N*-linked glycosylation sites in αIIb amino acid residues Asp-589, Gln-595, and Thr-478, which are located in the proximity of the α-genu region where the integrin folds backwards in the bent conformation. These residues are all located in the thigh domain (Fig. 3*A*). We have previously shown that swapping the entire thigh domain between αIIb and αV did not have a significant impact on the αIIbβ3-Fbg interaction (22). Among these residues, Gln-595 is located immediately behind the α-genu. When 595QTR[4] was mutated to 595NTT (Q595N/R597T), robust Fbg binding was observed in the presence of $Ca^{2+}/Mg^{2+}$, and the addition of PT25-2 did not significantly increase the binding. When the 589DTH sequence located distal to the α-genu region was mutated to 589NTT (D589N/H591T), it induced moderate Fbg binding, and PT25-2 significantly increased the binding. In contrast, when 478TKT, which is located above the α-genu region, was mutated to 478NKT (T478N), it did not affect Fbg binding at all (Fig. 3*B*). It is possible that these mutations affect ligand binding by directly altering the local structure of the αIIbβ3, regardless of the actual *N*-glycan binding. To rule out these possibilities, the 595QTR sequence was mutated. Mutating 595QTR to ATT, DTT, WTT, NTR, QTT, or NTA did not induce significant activation. However, mutating 595QTR to NTS induced activation

[4] 478TKT, 589DTH, and 595QTR designate wild-type αIIb sequences. The three letters following the number represent the amino acid residues starting from the position the number represents.